Hindawi
Journal of Nanomaterials
Volume 2023, Article ID 6353894, 23 pages
https://doi.org/10.1155/2023/6353894

Research Article

Characteristics and Electrochemical Performance of Hydroxyl-Functionalized Graphene Quantum Dot-Coated Si Nanoparticles/Reduced Graphene Hybrid Anodes for Advanced Li-Ion Batteries

Angelica Martino,[1] Ruye Cong,[1] Minsang Jo,[2] Hyun-Ho Park,[1] Hochun Lee,[2] and Chang-Seop Lee[1]

[1]*Department of Chemistry, Keimyung University, Daegu 42601, Republic of Korea*
[2]*Department of Energy Science and Engineering, DGIST, Daegu 42988, Republic of Korea*

Correspondence should be addressed to Chang-Seop Lee; surfkm@kmu.ac.kr

Received 14 November 2022; Revised 21 April 2023; Accepted 26 April 2023; Published 18 May 2023

Academic Editor: Dong Kee Yi

By powering sophisticated lithium-ion batteries (LIBs), silicon/carbon (Si/C) composites have the potential to accelerate the sustainable energy transition. This is a first-of-its-kind Si/C hybrid with hydroxyl-functionalized graphene quantum dots (OH-GQD) electrostatically assembled within interconnected reduced graphene oxide networks (OH-GQD@Si/rGO) prepared through solution-phase ultrasonication and subsequent one-step, low-temperature annealing and thermal reduction. The OH-GQD@Si/rGO hybrid utilized as the LIB anode delivered a high initial specific capacity of 2,229.16, 1,303.21, and 1,090.13 mAh g^{-1} reversible capacities at 100 mA g^{-1} after 50 and 100 cycles, and recovered 1,473.28 mAh g^{-1} at rates as high as 5 A g^{-1}. The synergistic benefits of the OH-GQD/rGO interface give dual, conductive carbon protection to silicon nanoparticles. Consecutive Si surface modifications improved Si–rGO contact modes. The initial OH-GQD carbon coating increased storage capacity through vacancy defects changing the electron density in the lattice, whereas hydroxyl functionality at the edges acted as active storage sites. Secondary protection through rGO encapsulation improved Si conductivity and usage by providing continuous electron/ion routes while minimizing Si volume variations. The proposed OH-GQD/rGO hybridization as a dual-carbon protection strategy to Si stabilized the solid electrolyte interface leading to electrode stability. This work is expected to advance the development of next-generation Si-based LIB anodes.

1. Introduction

Energy and the environment are critical issues in modern society's long-term growth [1]. The shift toward sustainable energy sources to reduce global carbon emissions has piqued many people in lithium-ion batteries (LIBs) as efficient, dependable electrochemical energy storage systems [2]. LIBs are the dominating technology for commercial applications such as portable electronic devices [3], emerging low- or zero-emission electric vehicles (EVs) and hybrid EVs [4], grid-scale energy storage [5], and medical devices [6] because of their comparatively high-energy and power density, outstanding cycle stability, high operating voltages with low self-discharge, lack of memory effects [7], and low maintenance requirements. However, commercial graphite anodes have a low specific capacity of 372 mAh g^{-1}, making them unsuitable for sophisticated high-power/high-energy-density batteries.

Silicon (Si) possesses an exceptionally high theoretical specific capacity 10 times than that of conventional graphite (4,200 mAh g^{-1} for $Li_{22}Si_5$) [8]. Si operates at a low discharge voltage that can lessen adverse Li plating processes; Si is environmentally benign, naturally abundant, and low in production costs [9]. However, its electrochemical performance is significantly hampered by its extreme volume expansion (~400% for $Li_{4.4}Si$), which causes high internal stress leading to pulverization of the Si morphology during repeated

lithiation–delithiation processes [10]. This promotes the isolation of Si, resulting in a loss of electrical contact between the conductive network and the current collector, which compromises electrical conductivity and battery efficiency [11, 12]. Continuing pulverization exposes more bare Si particles to the electrolyte, resulting in the recurrent creation of a structurally unstable solid electrolyte interface (SEI), which finally leads to rapid capacity decline and overall structural collapse [13]. Structure regulation of Si into nanostructures [14], thin films [15], nanotubes [16], nanowires [17], nanospheres [18], and nanoporous structures [19] have been reported to efficiently reduce internal mechanical stress on Si to ameliorate pulverization. However, the problem of excessive SEI formation remains. Furthermore, Si-based electrodes have limited electrical conductivity with slow reaction kinetics by design.

The use of carbon nanomaterials as a secondary phase, such as carbon coating, double-coating techniques, anchoring of active materials inside carbon layers, and encapsulation strategies to improve electronic conductivity and structural stability, leading to enhanced electrochemical performance of diverse electrode materials have been extensively reported. A 2D molybdenum carbide/nitride Mxene anode enhanced the charge storage mechanism through ordered vacancy defects, while Nb_2C Mxene cathode displayed remarkable K-ion storage and cycling capability [20, 21]. The two-pronged technique using a 3D carbon framework with an Al_2O_3 layer to limit electrolyte decomposition stabilized both SEI and cathode electrolyte interphase with enhanced interfacial stability [22]. $Ni_{1.8}Co_{1.2}Se$ nanoparticles covered with N-doped carbon (NDC) and encased in an NDC nano box exhibited high electrochemical performance at low-temperature climate attributed to 3D dual conductive networks promoting ultrafast ions/electron transport [23]. Synergistic effects of a double-carbon layer from gelatin-derived carbon and reduced graphene oxide (rGO) in $Na_3V(PO_4)_3$–$Na_3Fe_2(PO_4)(P_2O_7)$ composite [24] and a double-layer coating strategy in a Si@SiO_x@C-NB anode resulted in a superior rate capability of 690 mAh g^{-1} at 5 A g^{-1} [25]. O-containing groups from ball-milling of graphite oxide (GO) assisted in the in situ growth of LTO nanoparticles in nano-$Li_4Ti_5O_{12}$/reduced graphite oxide composite [26]. Similar to Si, manganese-based chalcogenides with innately low electronic conductivity demonstrated a notable capacity of 1,039 mAh g^{-1} over 100 cycles when electrostatically embedded in N-doped graphene (N–G) [27]. Inspired by twofold carbon protection techniques, initial carbon coating to Si and secondary carbon anchoring within graphene present a viable strategy.

Graphene possesses high electrical conductivity, excellent thermal and mechanical stability, with a sheet-like structure able to compensate for the low electrical conductivity of Si [28]. Si in 3D all-carbon conductive graphdiyne (GDY) networks delivered 4,122 mAh g^{-1} capacity [29]. Cage-shaped, defect-repaired rGO-supporting silicon nanoparticles (SiNP) produced a capacity of 2,678.4 mAh g^{-1} at 100 mA g^{-1} [30]. Si embedded in graphene demonstrated superior cycling stability with 1,516.23 mAh g^{-1} retained after 100 cycles [31]. After rGO encapsulation, porous Si nanostructures displayed an increased conductivity allowing a superior rate performance of 497 mAh g^{-1} at 2.0 C [32]. Carbon-coated SiNP enclosed in a 3D N–G matrix crosslinked with carbon nanofibers previously constructed by the authors delivered 1,371.4 mAh g^{-1} capacity with outstanding structural stability [33].

The enormous potential of Si/graphene-based systems for advanced battery applications is limited due to inherent Si and graphene characteristics. The difficulty in achieving a stable SiNP dispersion due to its hydrophobic nature originating from the native surface SiO_2 layer causes particle agglomeration and Si fallout under severe mechanical stress. Surface modification on SiNP using piranha solution to address problems on dispersibility via surface hydroxyl (OH) groups have been reported to significantly increase hydrophilicity crucial to a stable nanostructure assembly [34]. Meanwhile, the use of cationic surfactant poly(diallyldimethylammonium chloride) (PDDA) to modify SiNP induced strong hydrogen bonds between PDDA ammonium groups of PDDA and the O-containing groups of GO, thus facilitating SiNP grafting into GO [35]. The irreversible superimposition of graphene sheets due to strong van der Waals forces also hinders charge transfer kinetics. Due to size difference between nanoscale SiNP and typical microscale graphene, actual contact point at the heterointerface is reduced, and Li^+ ion tortuosity across huge graphene sheets is increased, inevitably leading to suboptimal Li^+ ion diffusion rates [36].

Graphene reduced to a few nanometers yields 0D graphene quantum dots (GQD) with intriguing physicochemical features due to quantum confinement and edge effects [37]. GQD have abundant active sites (edges, functional groups, and dopants) with exceptional dispersibility and tunability [38]. Photoluminescence can be tailored by attaching functional groups, and a bandgap can also be engineered, making it superior to its 2D graphene equivalent [39]. GQD combines the benefits of graphene and quantum dots with promising diverse applications such as supercapacitors [40], water splitting and CO_2 reduction electrocatalysts [37], LIBs, and other battery systems (P, K, and Na) [41, 42]. Interestingly, when combined with other carbon nanomaterials, GQD produces a synergistic effect on the electrochemical performance of LIBs. For instance, a functionalized GQD combined with a carbon nanotube matrix promoted a 700 mAh g^{-1} of capacity ascribed to active functionalities [38]. A hydroxyl (−OH)-functionalized GQD increased chemical reactivity induced by O-containing functionality as active sites with a strong affinity for Li^+ ions [43]. On the other hand, GQD as a coating material provided soft protection to CuO/Cu nanowires, assisted fast transport kinetics, and enhanced surface conductivity [42]. As a surface stabilizer, GQD prevented particle aggregation and generated a protective barrier to impede the dissolution of active materials [44–46]. In Si-based systems, GQD coating stabilized the SEI and delivered a high capacity of 3,068 mAh g^{-1} after 100 cycles [34]. Nevertheless, previous literatures only employed GQD as a surface stabilizer and a coating material with a small mass loading rather than as an active material.

In this study, we designed a facile two-pronged approach to synthesize a hybrid anode material using novel hydroxyl-functionalized GQD (OH-GQD) as a surface stabilizer to Si

and simultaneously as an active material partaking in electrochemical reactions. The composite fabrication comprises a two-part approach addressing: (1) Si low dispersibility; (2) poor electronic conductivity; (3) weak Si/graphene interface against Si volume changes; and (4) unstable SEI formation. Initial SiNP surface modifications were conducted using piranha solution and PDDA surfactant to attain a hydrophilic Si with excellent dispersibility. The first part of composite fabrication starts from the alkaline-phase hydrothermal synthesis of OH-GQD crystals. The second part describes the composite fabrication via electrostatic assembly using simple ultrasonication under optimum pH conditions. The double-carbon protection strategy to resolve Si challenges was successfully accomplished using an OH-GQD layer as an initial conductive carbon coating followed by GO encapsulation as a secondary carbon protection upon repeated lithiation/delithiation processes. The electrochemical properties of 0.2OH-GQD@Si/0.2rGO-1 and 0.3OH-GQD@Si/0.1rGO-2 hybrids as LIB anodes are then characterized. From all we know, the interplay between OH-GQD/rGO double-carbon hybridization as a conductive carbon protection technique to enhance the electronic conductivity and stability of SiNP and its influence on electrochemical performance has not been quantitatively probed.

The two-pronged approach follows a simplified fabrication process appropriate for industrial applications with multiple advantages. First, the OH-GQD coating compensated for the low conductivity of SiNP through vacancy defects and abundant −OH functional groups, which also function as storage sites for Li^+ ions. Second, consecutive surface modifications enhanced contact modes of SiNP with OH-GQD and rGO via induced hydrogen bonds. Third, the sheet-like structure of graphene provided a continuous transport network for effective electron–ion intercalation across the composite and offered a second barrier of protection to counter outward Si volume expansion, thereby improving overall electrode structural integrity. Lastly, the resultant hybrids were processed in a low-temperature, one-step OH-GQD annealing vis-à-vis rGO thermal reduction, hence simplifying processing operations.

2. Materials and Methods

2.1. Materials and Reagents. The reagents employed in the research were of analytical grade and utilized as obtained with no further purification. Sulfuric acid (H_2SO_4, 98%) and hydrogen peroxide (H_2O_2, 30%) were purchased from Daejung Chemicals & Metals. Pyrene ($C_{16}H_{10}$, 98%), PDDA ($(C_8H_{16}NCl)_n$, 35%), and ethyl alcohol (anhydrous, 99.9%) were purchased from Sigma Aldrich. Si nanoparticles (powder, APS $\leq$ 50 nm, 98%) were purchased from Alfa Aesar. A Commercial GO dispersion solution (N002-PS, 0.5%) purchased from Angstron Materials was used as obtained. All the aqueous solutions in the experiments were prepared with deionized (DI) water.

2.2. Materials Preparation

2.2.1. Fabrication of OH-GQD. The resultant composites were prepared following the proposed two-pronged strategy starting from OH-GQD synthesis in line with the work of Wang et al. [47] with minor modifications. In detail, OH-GQD were synthesized from the molecular fusion of a carbon precursor acquired from the nitration of the relatively less toxic pyrene (than polyaromatic hydrocarbons) into 1,3,6-trinitro pyrene in a reflux reaction at 80°C for 12 hr. The refluxed solution was then diluted using 1 L of DI water and then vacuum-filtered by washing the filtrates with DI water numerous times to eliminate excess acid. Yellow powder was yielded after oven-drying at 80°C for 24 hr. The produced yellow powder was dispersed in a 0.6 L of 0.2 M NaOH solution via ultrasonication for 2 hr, followed by hydrothermal treatment in a sealed, Teflon-lined autoclave. The hydrothermal processing allowed the catalyst-free, alkaline phase-assisted molecular fusion of pyrene molecules and the graphitized carbon material in the presence of a strongly basic aqueous medium, thereby eliminating the nitrate groups from the 1,3,6-trinitro pyrene structure. This was followed by the molecular fusion of the pyrene molecules into single-crystal OH-GQD at a considerably low temperature of 200°C for 12 hr. Following this reaction, the yielded black colloidal solution of OH-GQD was cooled to room temperature and then subjected to vacuum filtration in a 0.22 μm membrane to extract unreacted solid carbon precipitates. The colloidal OH-GQD solution underwent dialysis in a dialysis bag submerged in DI water for 2 days with constant water replacement to dissolve salts produced during pyrolysis. The colloidal OH-GQD solution was obtained in the form of black powder for further characterization.

2.2.2. Fabrication of 0.2OH-GQD@Si/0.2rGO-1 and 0.3OH-GQD@Si/0.1rGO-2 Composites. The second phase of the proposed composite fabrication strategy comprises the solution phase, consecutive surface modification of SiNP, facile ultrasonication-assisted OH-GQD coating, and subsequent GO anchoring to provide a double-carbon protection layer to Si via stimulated electrostatic assembly, to a one-step, low-temperature OH-GQD annealing, and rGO thermal reduction process, as shown in Figure 1.

In summary, the composite fabrication process initiated with solution-phase and consecutive surface modifications conducted on SiNPs. The initial surface modification was conducted to address the Si hydrophobic nature by diffusing 4.0 g of SiNP in a typical piranha solution (H_2SO_4/H_2O_2, 3 : 1 v/v) and storing at 80°C under constant stirring for 6 hr to complete the reaction process. This process allowed abundant −OH groups supplied by the acidic medium to be grafted onto the surface of Si to yield SiOH, thereby improving hydrophilicity. The excess acid was eliminated employing a 0.22 μm membrane, and the resultant SiOH nanoparticles were washed with DI water severally to remove the remaining piranha solution. The resulting SiOH was dried in a vacuum oven at 80°C for 24 hr and obtained as a fine, brown powder for material characterization.

A secondary surface modification was conducted on SiOH in preparation for the ultrasonication-assisted composite fabrication through electrostatic assembly, detailed as follows: 0.04 g of the obtained SiOH powder was dispersed

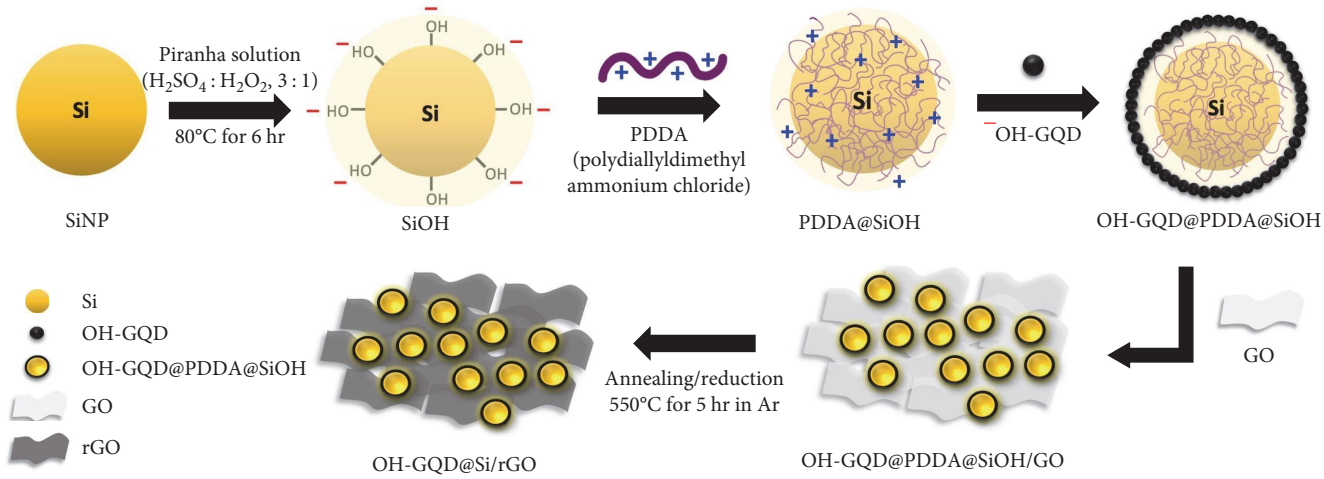

Figure 1: Schematic representation of the fabrication process of OH-GQD@Si/rGO.

in 0.3 L DI water via ultrasonication for 2 hr. Strong electrostatic interactions between composite parts (i.e., SiOH, OH-GQD, and GO) with optimized colloidal stability identified by zeta potential values and computed isoelectric point (IEP) were stimulated via dropwise addition under vigorous stirring of 35 wt% PDDA. This secondary surface modification on SiOH was conducted to contribute to electrostatic interactions between major composite parts by initiating strong hydrogen bonds between the N atoms found in the PDDA structure and the oxygen-containing groups abundant in OH-GQD and GO carbon nanomaterials. Following 1 hr of ultrasonication, a PDDA-surface-modified SiOH (PDDA@SiOH) solution was attained. The prepared colloidal OH-GQD solution, oven-dried and collected in the form of black powder, was then added to the PDDA@SiOH solution. The mixture was ultrasonicated for 2 hr to induce the electrostatic assembly and constantly stirred for another 6 hr to complete the electrostatic assembly between charged particles to yield the OH-GQD@PDDA@SiOH solution. Lastly, 0.02 L of a 0.5 g L^{-1} of GO dispersion solution was added in a dropwise manner to the OH-GQD@PDDA@SiOH solution, followed by ultrasonication for 2 hr to yield OH-GQD@PDDA@SiOH/GO solution.

To describe the synergistic effect of the proposed OH-GQD coating and GO anchoring as a double protection strategy to address Si volume expansion and to measure the interplay between OH-GQD/rGO hybridization, electrochemical performance, and overall stability, two composites materials with different weight ratios were fabricated following the aforementioned procedure to yield a composite colloidal solution of 0.2OH-GQD@PDDA@SiOH/0.2GO-1, with OH-GQD/GO = 1 : 1 ratio prepared using 0.04 g SiOH, 0.02 g OH-GQD, and 0.04 L GO dispersion; and 0.3OH-GQD@PDDA@SiOH/0.1GO-2, with OH-GQD/GO = 2 : 1 ratio, synthesized using 0.04 g SiOH, 0.3 g OH-GQD, 0.02 L GO dispersion. The amount of SiOH regarding the total amount of carbon nanomaterials (e.g., OH-GQD and GO combined) is kept at a 1 : 1 ratio. The composite colloidal solutions were then dried in a vacuum oven at 80°C for 24 hr and obtained as powders. Lastly, the composite powders underwent low-temperature, one-step vis-à-vis OH-GQD annealing and rGO thermal reduction in a tube furnace employing high-purity Ar gas with a controlled gas flow rate of 500 standard cm^3 min^{-1} at a temperature ramp rate of 10°C min^{-1} until the maximum set temperature of 550°C, where the powders were stored for 5 hr to yield 0.2OH-GQD@Si/0.2rGO-1 and 0.3OH-GQD@Si/0.1rGO-2 as the final composites.

2.3. Materials Characterization. The structural and morphological characteristics of the fabricated OH-GQD@Si/rGO composites were examined by scanning electron microscope (SEM, S-4800, Hitachi, Tokyo, Japan) at 100 kV and transmission electron microscope (TEM, JEM-2100, JEOL, Tokyo, Japan). The successful electrostatic assembly of charged composite component particles was provided by collecting the zeta potential values employed to identify the IEP and sufficient pH range of composite parts for optimum stability of electrostatic assembly using a particle size analyzer (Zetasizer Nano ZS, Malvern Instruments Limited., Worcestershire, UK). Qualitative and quantitative microanalysis of the elements of the prepared hybrid materials were conducted by energy-dispersive X-ray spectroscopy (EDX, ARL-3460, Thermo Fisher Scientific, Waltham, MA, USA). The sample compositions and crystalline structures were characterized via powder X-ray diffraction (XRD) measurements utilizing a 2 kW Ultima IV (Rigaku, Tokyo, Japan) with Cu–Kα radiation ($K = 1.5418$ Å) at $2\theta = 2°–90°$. Raman spectra were acquired using a Jobin–Yvon LabRAM HR-800 (Horiba, Kyoto, Japan) with laser light ($\lambda = 514$ nm) at wavelengths of 100–3,000 cm^{-1}. Fourier-transform infrared spectroscopy (FTIR) was conducted using KBr pellets at frequencies of 4,000–500 cm^{-1} using a Nicolet 6700 spectrophotometer (Thermo Fisher Scientific, Waltham, MA, USA). X-ray photoelectron spectroscopy (XPS, Multilab-2000, Thermo Fisher Scientific, Waltham, MA, USA) analysis was carried out on an Al-Kα twin-anode X-ray source. The specific mass loadings of SiNP and carbon nanomaterials present in the composites were computed according to the thermogravimetric analysis

(TGA) curves collected using a Diamond TG/DTA system (PerkinElmer, Waltham, MA, USA) from 25 to 800°C at a heating rate of 10°C min^{-1} in air. Furthermore, the surface and cross-sectional view of the assembled coin cell electrode materials were characterized utilizing SEM (S-4800, Hitachi, Tokyo, Japan) at 100 kV to identify the topological structure and degree of electrode-volume expansion following 50 lithiation/delithiation cycles. To evaluate the crystalline structure of the composite material thinly coated at the Cu foil and to reduce high-intensity Cu peaks observed from normal XRD analysis conducted at $2\theta = 2°-90°$, XRD thin film analysis was performed for the Cu film in a low-incident beam at a fixed angle of $2\theta = 1°$.

2.4. Electrochemical Testing. The formulated 0.2OH-GQD@Si/0.2rGO-1 and 0.3OH-GQD@Si/0.rGO-2 hybrid nanomaterials were employed as active anodic materials in a two-electrode battery system. To assess the electrochemical performance of the two composite materials, a conventional slurry procedure was applied to fabricate working electrodes employing a mixture comprising 80 wt% of the respective composite sample as active materials, 10 wt% super P carbon black as the conductive agent, and 10 wt% polyvinylidene fluoride (PVDF) as the binder. The prepared slurry was cast on a copper (Cu) foil and dried in a vacuum oven at 60°C for 24 hr to yield the electrode plate. Circular disks with a diameter of 14 mm were punched from the electrode plate while keeping an ~1 mg cm^{-2} average load density for each electrode disk. Metallic Li foil was employed as the counter/reference electrode; a standard polyethylene membrane (Celgard 2600) was the chosen separator; a 1 M $LiPF_6$ solution dissolved in a mixture of ethylene carbonate, dimethyl carbonate, and ethyl methyl carbonate (EMC) (1 : 1 : 1 v/v) was employed as the typical electrolyte solution. The components of the two-electrode battery system were assembled in a coin cell-type battery (CR2032) inside a glove box filled with high-purity Ar gas to avert the corrosion of the metallic Li foil counter electrode. High-rate loading tests, such as galvanostatic charge/discharge profile measurements, were carried out on the developed coin cells using a battery tester (Neware Co., Ltd. Shenzhen, China) at voltages of 0.01 – 1.5 V (vs. Li/Li^+). The specific capacity was computed following the mass loading of the anode material in the electrode disk. Cyclic voltammetry (CV) was conducted at a scan rate of 0.1 mV s^{-1} at voltages of 0.01 – 1.5 V at 25°C. Electrochemical impedance spectroscopy (EIS) measurements were carried out on a Chi 660D electrochemical analysis instrument (CH Instruments, Inc. Shanghai, China) at frequencies of 100 kHz to 10 mHz and an amplitude of 5 mV.

3. Results and Discussion

3.1. Dual Surface Modifications of SiNP into SiOH and PDDA@SiOH. Figure 2 depicts evidence of successful surface modification performed on SiNPs. As-received ~50 nm SiNPs (Figure 2(a)) developed a distinct surface roughness ascribed to the polymer chains of PDDA (Figure 2(b)). The EDS mapping image (Figure 2(c)) illustrating the uniform scattering of Cl and N atoms on the surface also verifies the successful consecutive surface modifications of SiOH into PDDA@SiOH using PDDA surfactant (Figure S1). Additional evidence of successful SiNP surface modifications and composite electrostatic assembly stability of the components were supplemented by zeta potential values at various concentrations based on sample particle size (Table S1) and IEP determination at pH 2 – 12 (Table S2). Initial piranha solution treatment to SiNP presented a significant amount of −OH groups at the surface to produce hydrophilic SiOH (−38.5 mV) with improved hydrophilicity permitting a uniformly dispersed Si in aqueous solutions [34]. The EDX mapping also validated abundant O atoms following piranha treatment. The surface modifications carried out on the SiNP before the electrode assembly was also supervised via FTIR. Figures 2(d) and 2(e) compares the spectra of the pristine Si, hydrophilic SiOH nanoparticles, and PDDA@SiOH. The spectra of the as-received Si sample are similar to those of the piranha-treated SiOH sample, exhibiting a broad peak at 1,000 – 1,300 cm^{-1}, a characteristic strong band at 1,080 cm^{-1} (related to Si–O–Si symmetrical vibrations), a shoulder peak at 1,170 cm^{-1} (ascribed to Si–O–Si asymmetrical stretching signals), and a broad adsorption band at 3,000–3,600 cm^{-1} (centered at 3,340 cm^{-1} and corresponding to −OH stretching vibration) [33]. Figure 2(d) shows a dramatic increase in the surface −OH groups of the piranha-treated SiOH nanoparticles. Additional surface modification of SiOH nanoparticles using PDDA molecules into PDDA@SiOH is presented in the characteristic broad C–N stretching peak at 1,105 cm^{-1}, the appearance of two peaks between 1,500 and 1,750 cm^{-1}, and the presence of another peak at ~1,640 cm^{-1}, all ascribed to the wavelength of C=C groups provided to PDDA molecules (Figure 2(e)) [48]. The FTIR outcomes are consistent with the XPS results in Figures 2(f) and 2(g), where the peaks in the high-resolution Cl 2p and N 1s scans verify the success of the dual surface modifications carried out on SiNP before the electrode assembly essential to address Si low dispersibility owing to hydrophobic nature and inherently weak interfacial interaction with OH-GQD and GO.

3.2. Characterization of the Fabricated OH-GQD. Figure 3 illustrates evidence corroborating the successful fabrication of OH-GQD. Following the TEM results, OH-GQD is well dispersed, possessing a typical spherical shape (Figure 3(a)). The in-plane lattice fringe of an isolated OH-GQD crystal is 0.2397 nm, which is in line with the (100) plane of graphite (Figure 3(b)) [8]. The inset in Figure 3(b) shows a corresponding fast Fourier transform (FFT) pattern, which verifies that OH-GQD is a single-crystal graphene structure. Distinguishable benzene structures organized in an orderly, honeycomb-like carbon ring network characteristic of graphene confirm the crystallinity of the OH-GQD (Figure 3(c)). Moreover, the TEM outcomes gave insights into the edge geometry of OH-GQD. In general, a GQD can have three edge geometries: zigzag, armchair, or a combination of both geometries; each type considerably influences the shape and hence the electronic and optical properties of GQD (Figure S2) [49, 50]. The OH-GQD crystal in Figure 3(c) demonstrates the dominance of the zigzag edge geometry along the red arrows with

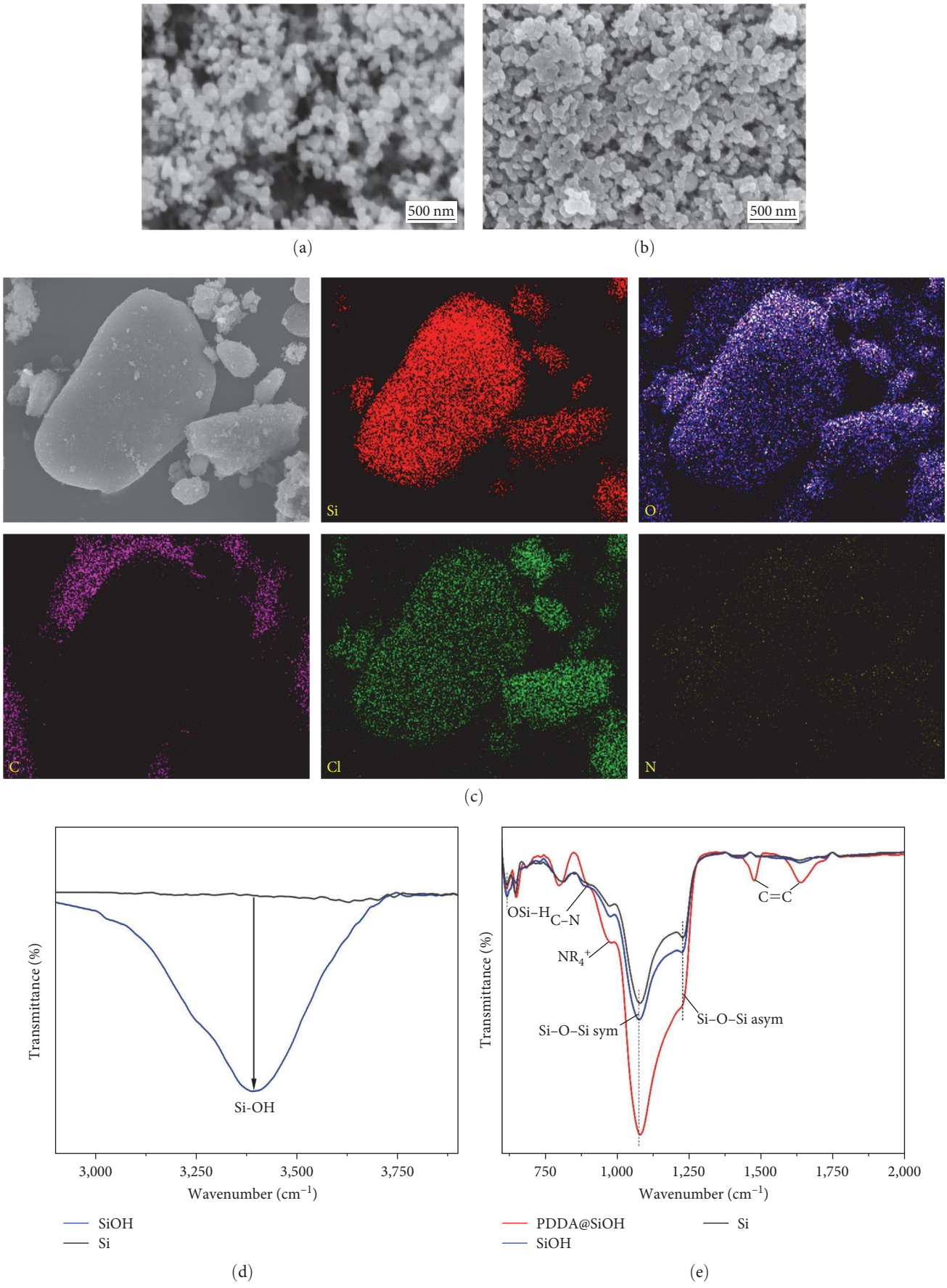

Figure 2: Continued.

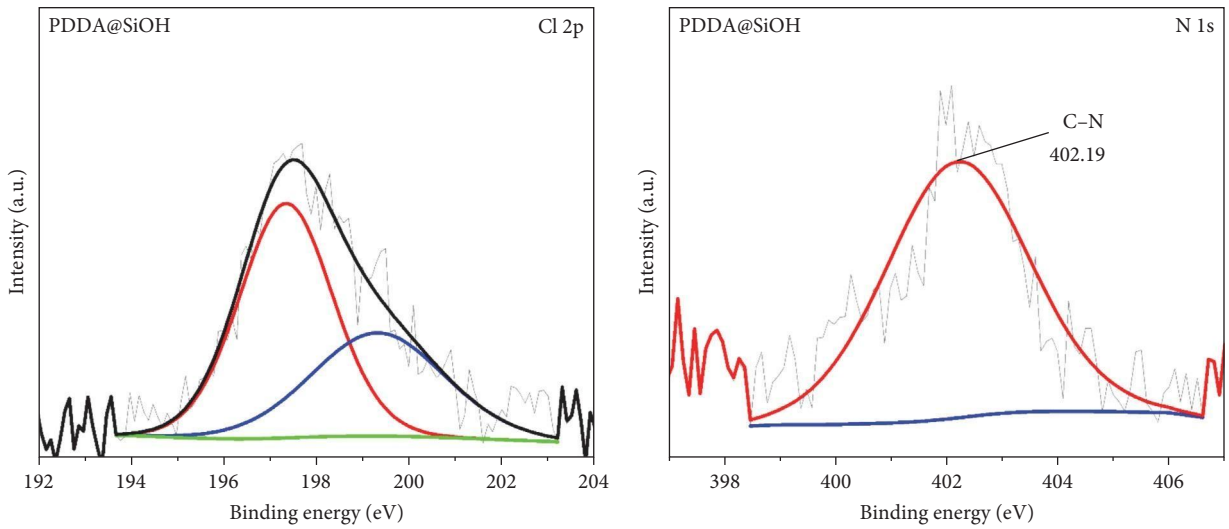

FIGURE 2: SEM images of pure SiNP (a), SiOH following piranha treatment (b), and EDX of PDDA@SiOH after PDDA modification (c), FTIR outcomes comparing SiNP, SiOH (d), and PDDA@SiOH (e), high-resolution Cl 2p (f) and N 1s (g) spectra of PDDA@SiOH.

inherent vacancy defects observed within the basal plane and along its edges. Generally, the zigzag edge geometry is ideal because it has better stability and electrocatalytic activity than the armchair or combined armchair-and-zigzag edge geometries [51]. The selected area electron diffraction (SAED) image of a single-crystal OH-GQD along the (001) zone axis demonstrates two diffraction rings ascribed to the (002) and (110) GQD basal planes of graphene (Figure 3(d)) [37]. The OH-GQD possesses a homogeneous lateral size of 1–4 nm with an average lateral size of 2.397 nm (Figure 3(e)).

XRD assessment compared the crystalline structure of OH-GQD with GO and rGO (Figure 3(f)). The spectrum of the fabricated OH-GQD exhibited a broad diffraction peak at $2\theta = 26°$ of similar quality to rGO, which is in line with the (002) plane of graphitic carbon nanomaterials attributed to a few-layered graphene sheet [52]. Likewise, the similarity between rGO and OH-GQD spectra shows the successful construction of a graphitic network structure following alkaline medium-assisted molecular fusion of pyrene precursor into crystalline OH-GQD. Applying Bragg's law, $\lambda = 2d \sin\theta$ where is wavelength λ of the X-ray radiation employed to irradiate the sample, d denotes the spacing between the lattice planes, and θ represents the measured diffraction angle, the interlayer spacing of the OH-GQD was estimated (3.34 Å) and was observed to correspond to that of bulk graphite, which suggests that OH-GQD possess a high degree of graphitization [47, 53].

Raman spectroscopy outcomes validated that OH-GQD exhibits a high degree of graphitization, which portrayed a characteristic disordered D band at ~1,350 cm^{-1} and ordered G band at ~1,590 cm^{-1} typical of graphite and other sp^2-bonded carbons (Figure 3(g)). In the interim, the I_D/I_G ratio of OH-GQD (0.86) is similar to those of the minimized composites and slightly higher than that of rGO (0.85). This presents a validation of the existence of vacancy defects within OH-GQD's graphitic lattice initially seen in TEM analysis (Figure 3(c)) ascribed to the −OH functional groups attached at lattice edges. The −OH functionalities attached to the GQD lattice are also confirmed by the enlarged FTIR spectra in Figure 3(h), where a sharp peak attributed to C–OH is detected at 1,270 cm^{-1} in the IR region [47]. Additionally, the presence of a strong, broad vibration ascribed to the O–H bond at 3,400 cm^{-1} verifies the successful −OH functionalization of the GQD. The presence of −OH functionality of the synthesized GQD is also validated by high-resolution O 1s (Figure 3(i)) and C 1s (Figure 3(j)) XPS spectra. A broad peak at 286.47 eV for C 1s, similar to C–OH bonds, appears at 531.92 eV for O 1s, strongly suggesting the successful −OH functionalization [47]. Meanwhile, the C–C/C=C peak has exhibited a slight peak shifting from the standard graphitic C–C, which is 248.8 eV, to a higher binding energy of 284.93 eV as an outcome of −OH functionalization. The electrophilic O atoms of the hydroxyl groups with higher electronegativity attracted more electrons from the GQD graphitic C–C/C=C lattice, thus shifting the electron density toward the O atoms.

3.3. Structural and Morphological Characterizations of 0.2OH-GQD@Si/0.2rGO-1, and 0.3OH-GQD@Si/0.1rGO-2 Composites. Figure 4 shows the SEM images of 0.2OH-GQD@Si/0.2rGO-1 and 0.3OH-GQD@Si/0.1rGO-2 at different magnifications. In general, the nature of adhesion between Si and sp^2 carbons of GO is inherently weak, which causes the detachment of SiNP from the surface of GO, leading to capacity loss. Hence, various amounts of OH-GQD were employed to address SiNP/GO weak interfacial interactions and to inhibit the agglomeration of GO into irreversibly stacked layers commonly occurring in Si-based composites owing to strong van der Waals forces. Varying the OH-GQD:GO content during composite fabrication significantly influenced the coating efficiency of the GO

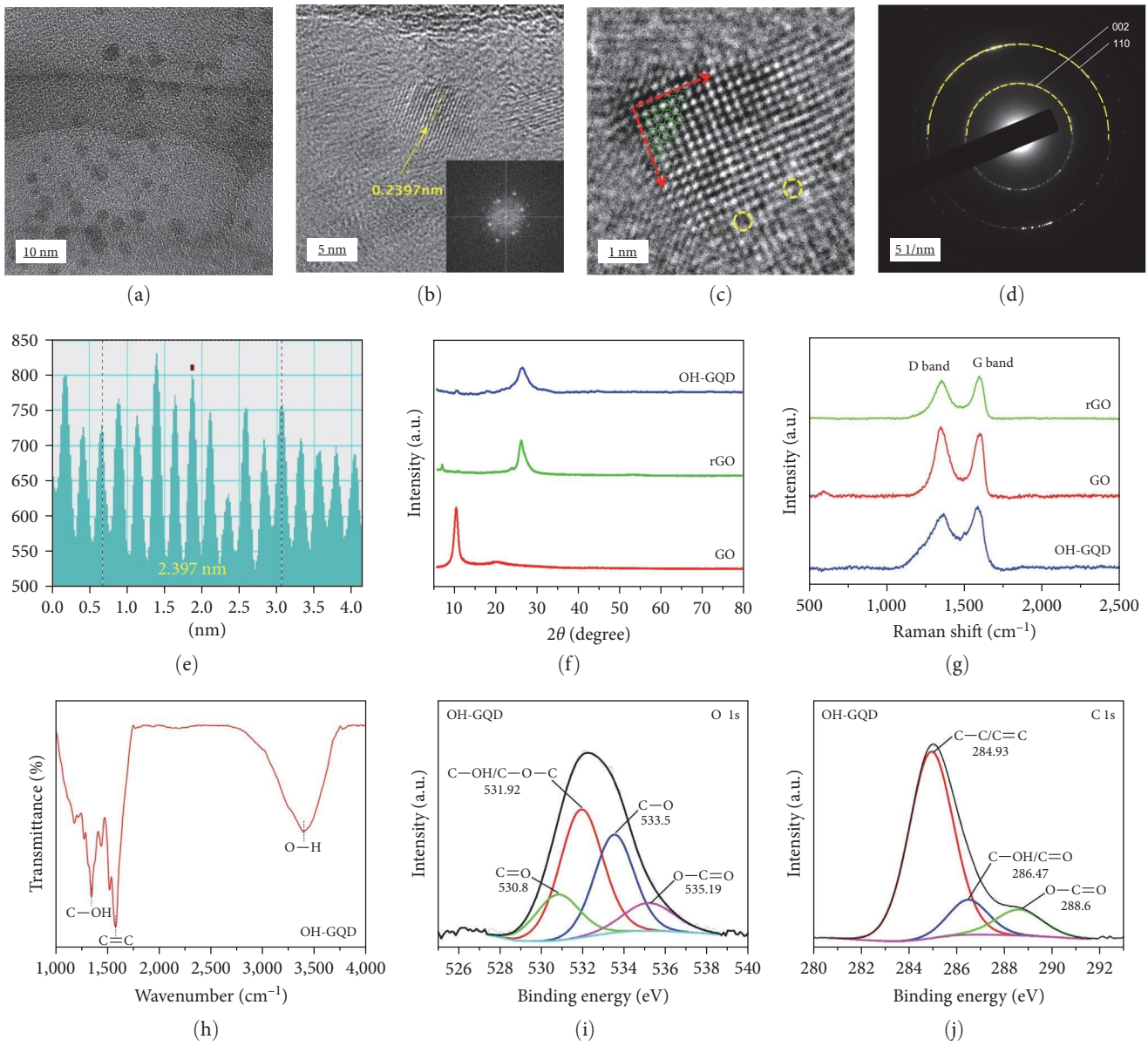

Figure 3: TEM images of fabricated OH-GQD at various magnifications (a–d) and corresponding height distribution profile (e); XRD pattern (f) and Raman spectra (g) of OH-GQD in comparison with GO and rGO; FTIR spectrum (h); and high-resolution O 1s (i) and C 1s (j) spectra.

sheets. Both composites have porous structures, which are denoted by the dark areas scattered across the composites in Figures 4(a) and 4(d). Contrarily, numerous bare SiNPs showing severe aggregation were exposed on the 0.2OH-GQD@Si/0.2rGO-1 surface, revealing a less efficient Si:GO coating ratio (Figures 4(b) and 4(c)). This issue is substantially lowered in the 0.3OH-GQD@Si/0.1rGO-2 composite, where most SiNPs are encapsulated within thin GO coating (Figures 4(e) and 4(f)). Weak adhesion at the SiNP/GO interface, GO agglomeration, and Si:GO coating ratio inefficiency can be resolved by placing a thin OH-GQD layer on the PDDA@SiOH particle surface before the assembly with GO.

Furthermore, the surface modification of SiOH into PDDA@SiOH, OH-GQD coating, and GO anchoring via electrostatic assembly was also supervised by identifying the zeta potential of the colloidal samples (Figure S3) and computing its IEP at a given concentration (Figure S4) before the composite assembly. Compared to the simple mechanical mixing of Si and GO, the surface modification presented by cationic PDDA not only affords OH-GQD coating to SiOH but also allows strong interfacial contact with GO sheets due to the strong electrostatic attraction between opposing charges. Furthermore, consecutive PDDA cationic surface treatment to hydrophilic SiOH was carried out to coat SiOH with a positive charge necessary to facilitate the electrostatic assembly with OH-GQD (−48.5 mV) and GO (−52.0 mV). Upon adding PDDA, the zeta potential values shifted to the positive scale for PDDA@SiOH (+57.6 mV), OH-GQD@PDDA@SiOH (+52.6 mV) and OH-GQD@PDDA@SiOH/GO (+49.4 mV). It is generally accepted that the zeta potential value of a colloidal suspension is sensitive

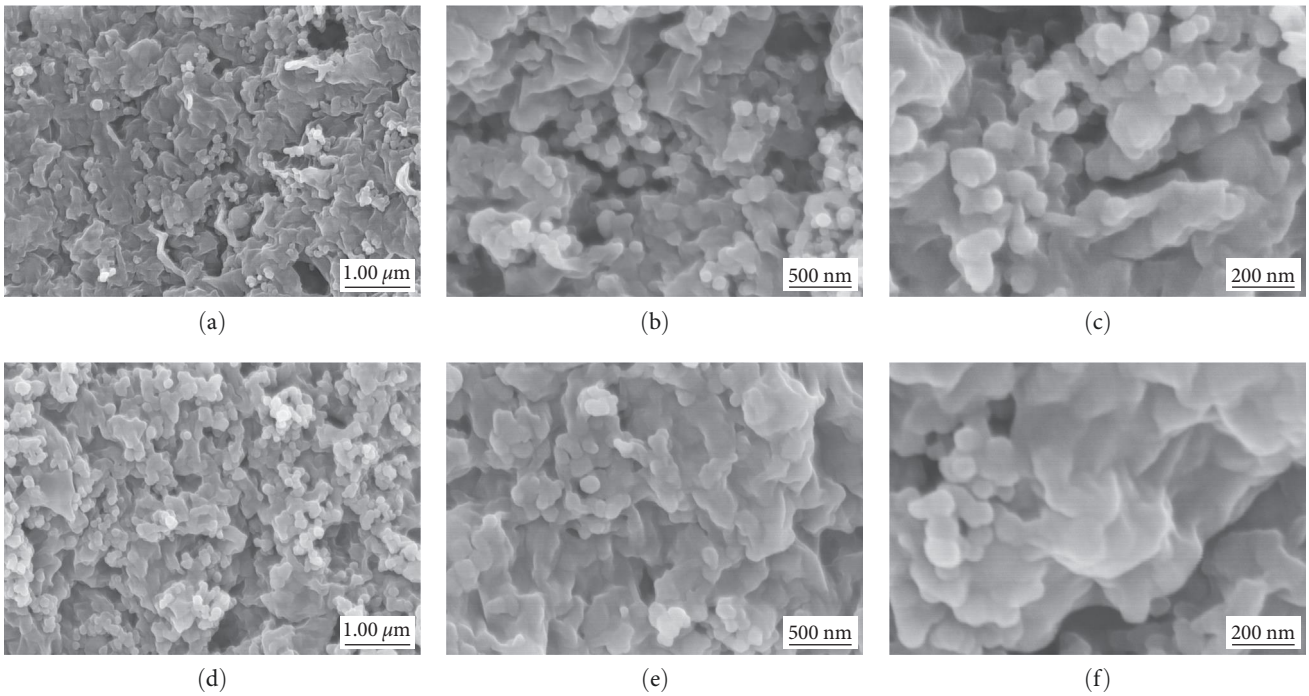

FIGURE 4: SEM images of 0.2OH-GQD@Si/0.2rGO-1 (a–c) and 0.3OH-GQD@Si/0.1rGO-2 (d–f) at different magnifications.

to pH changes. Furthermore, a zeta potential of +30 and −30 mV are thought of as stable dispersions, i.e., a stable electrostatic assembly of charged particles is possible. It should be noted that GO has a zeta potential above −30 mV at all pH values, which shows that colloidal stability is steady and will proceed to assemble with PDDA@SiOH and OH-GQD illustrated in Table S1 considering the dilution level per sample size. Consequently, electrostatic assembly for the resultant composite samples was executed at room temperature at the pH range of 6–8 for optimum conditions to aid the electrostatic assembly of PDDA@SiOH, OH-GQD, and GO particles (Table S2).

The presence of OH-GQD in the resultant composites unobserved by SEM was revealed by TEM analysis (Figure 5). The successful encapsulation of PDDA@SiOH particles by GO initially observed in the SEM images is additionally evidenced by the appearance of folded rGO sheets enveloping SiNP spheres in 0.2OH-GQD@Si/0.2rGO-1 (Figures 5(a) and 5(c)) and 0.3OH-GQD@Si/0.1rGO-2 (Figures 5(b) and 5(d)). The former, which has higher GO content, can be characterized by relatively greater SiNP agglomeration verified by dark spots with color intensity showing the extent of SiNP agglomeration (Figure 5(c)). Meanwhile, less agglomeration is detected in the latter composite, which by contrast, has higher OH-GQD content (Figure 5(d)). Consistent with the SEM and zeta potential measurement results, TEM analysis confirmed that an efficient Si:GO coating ratio was achieved in 0.3OH-GQD@Si/0.1rGO-2 ascribed to its high OH-GQD loading, which created a stable carbon coating on the PDDA@SiOH surface while improving interfacial interactions at SiNP/GO interface. Additionally, Figures 5(e) and 5(f) indicate three distinct highly ordered lattice spacings: 0.31 nm, which is attributed to the (111) plane of Si; 0.19 nm for rGO, similar to the (002) plane of graphene; and 0.24 nm for the OH-GQD, which is correlated with the lattice fringe value of graphene (1120) [40]. Remarkably, the lattice spacing of OH-GQD remained unchanged after electrostatic assembly into the studied composites. Furthermore, insights into the crystalline structure of 0.3OH-GQD@Si/0.1rGO-2 composite are evidenced by SAED image (Figure 5(g)) demonstrating vivid diffraction rings determined for the (111), (022), (004), (113), and (133) facets of face-centered cubic structure of Si crystals, while the (002) facet is assigned to the basal plane of the hexagonal crystalline graphene [54]. The diffraction rings of the composite match the real-time FFT pattern (Figure 5(h) inset), where distinct bright spots detected additionally suggest high crystallinity of the representative 0.3OH-GQD@Si/0.1rGO-2 composite.

XRD was employed to acquire a deeper understanding of the crystalline structure of the respective components and fabricated composites (Figure 6(a)). The thermal reduction caused the removal of −C–O–C−, C=O, −OH, and –COOH inherent within the basal planes and edges of GO. This is verified in the appearance of a characteristic strong and broad peak centered at $2\theta = 10°$ in GO, which eventually disappeared in rGO with a re-emergence of a broad peak at $2\theta = 25°$ attributed to the characteristic peak of amorphous C (002). Removing O-containing functional groups led to reducing the interlayer spacing between stacked GO sheets, thus shifting the diffraction angle to $2\theta = 25°$ [30, 55]. Intense diffraction peaks at $2\theta = 28.4°$, 47.3°, 56.1°, 69.1°, and 76.4° are seen in Si, which are indexed to the (111), (220), (311), (400), and (331) facets typical for a face-centered cubic Si crystal (Reference code 98-065-2265; Figure S18). These representative Si peaks are all found in the resultant composites suggesting that Si surface

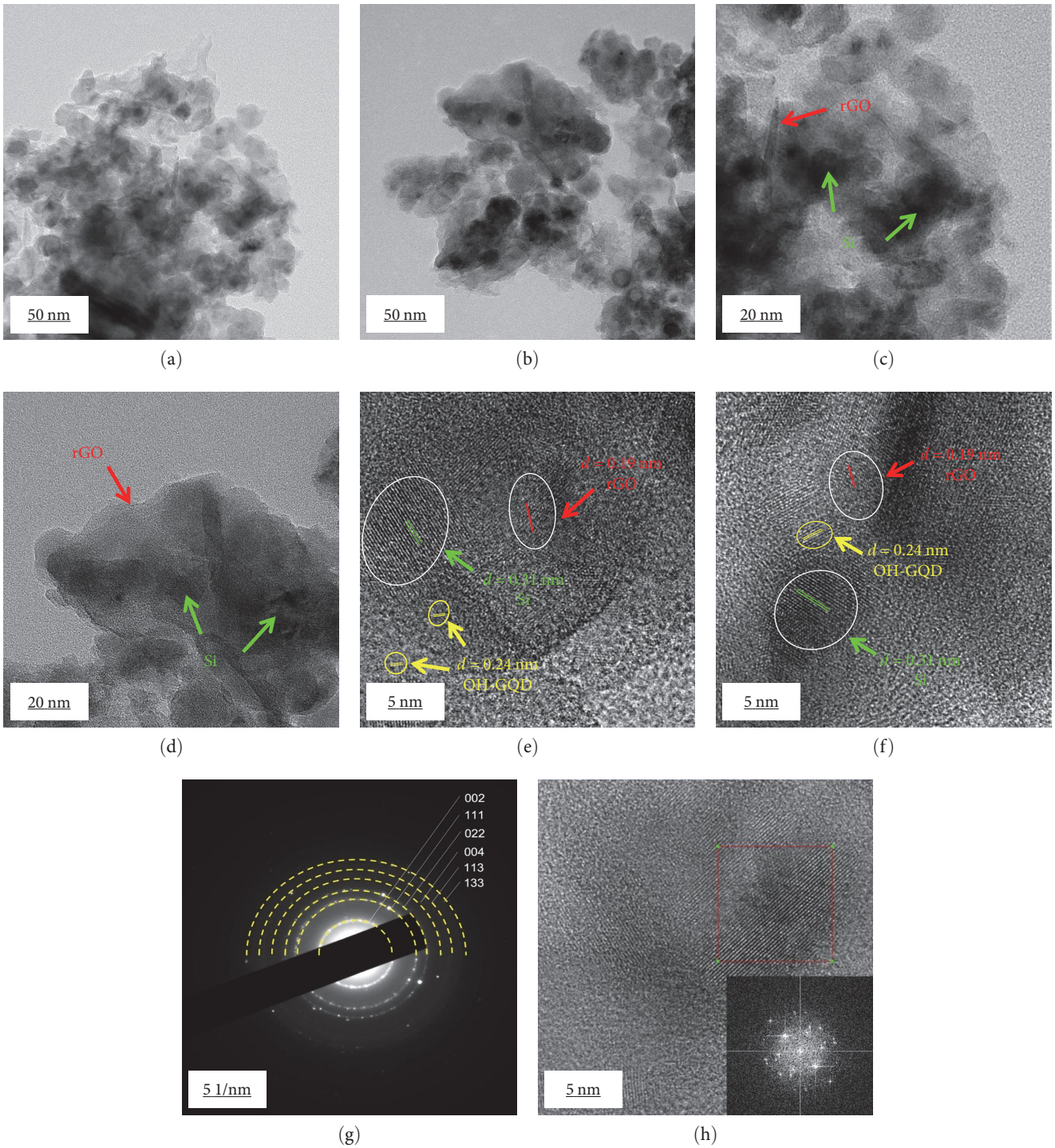

FIGURE 5: TEM images of 0.2OH-GQD@Si/0.2rGO-1 (a, c, e) and 0.3OH-GQD@Si/0.1rGO-2 (b, d, f) at different magnifications demonstrating individual lattice spacing assigned to Si, OH-GQD, and rGO (e, f). High crystallinity was verified by the SAED image (g) and representative FFT pattern (h inset) of 0.3OH-GQD@Si/0.1rGO-2.

modifications did not substantially alter its crystallinity. Additionally, the minimized composites exhibited diffraction peaks at $2\theta = 31.8°$ attributed to the (002) plane of graphene (2.82 Å) and a secondary peak at $2\theta = 45.5°$ indexed to the (022) plane of a cubic carbon oxide crystal (1.99 Å) (Reference code 98-002-6962; Figure S19).

The degree of graphitization, such as the presence of defects within internal structures, was assessed using Raman spectroscopy (Figure 6(b)). All samples portrayed a characteristic disordered D band at ~1,350 cm^{-1} and an ordered G band at ~1,590 cm^{-1}, typical of graphite and other sp^2-bonded carbons [56]. Remarkably, high intensities of the G bands compared to

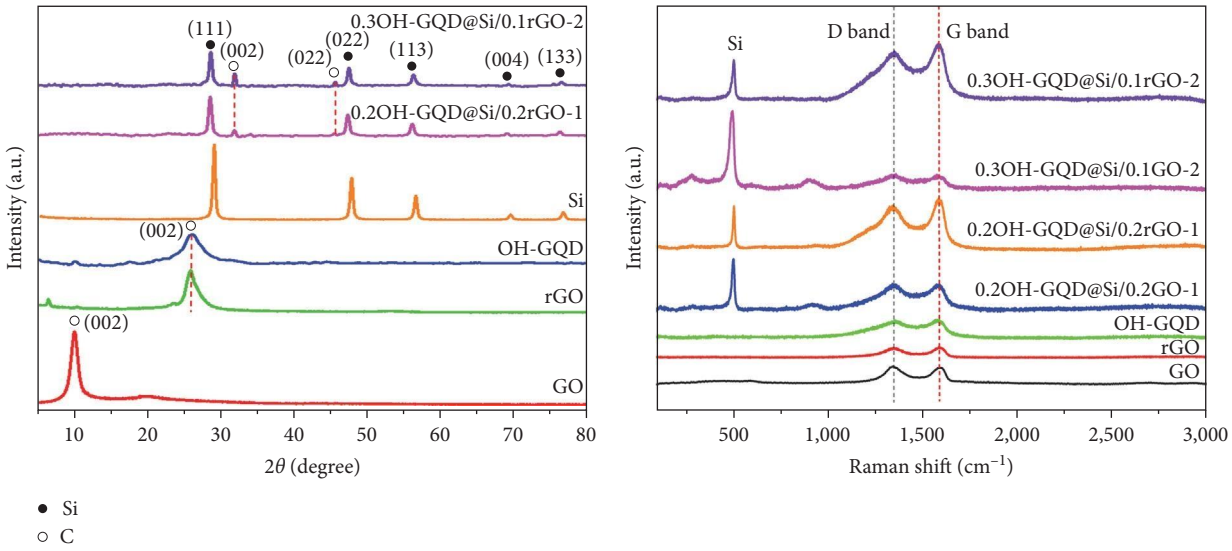

FIGURE 6: XRD patterns (a) of GO, rGO, OH-GQD, Si, 0.2OH-GQD@Si/0.2rGO-1, and 0.3OH-GQD@Si/0.1rGO-2. Raman spectra (b) of GO, rGO, OH-GQD, 0.2OH-GQD@Si/0.2rGO-1, and 0.3OH-GQD@Si/0.1rGO-2, including corresponding spectra before thermal annealing/reduction.

D bands of both 0.2OH-GQD@Si/0.2rGO-1 and 0.3OH-GQD@Si/0.1rGO-2 composites are strong indications of an integrated graphitic nature with excellent crystallinity and inherent few vacancy defects aligned with TEM findings. To characterize the defect quantity in the samples, the relative intensity ratio of the disordered carbon to the graphitized carbon (I_D/I_G) was quantified after curve fitting utilizing the Gaussian–Lorentzian model shown in Figures S5–S11 with corresponding I_D/I_G ratios, including fitting parameter values depicted in Table S3 [54, 57]. The increase in the I_D/I_G value of GO (0.84) following thermal reduction into rGO (0.85) is ascribed to the increase of O-terminated sp^2 carbon-edge atoms, consequently decreasing in-plane sp^2 graphitic domains [55]. A similar increasing I_D/I_G pattern is detected in 0.2OH-GQD@Si/0.2GO-1 (0.85) and 0.3OH-GQD@Si/0.1GO-2 (0.85) prior to reduction into 0.2OH-GQD@Si/0.2rGO-1 (0.86) and 0.3OH-GQD@Si/0.1rGO-2 (0.86), respectively. Furthermore, intensities and peak areas under respective curves of D and G bands for both composites are dramatically elevated before and after thermal reduction. Meanwhile, OH-GQD (0.86) is with a defect quantity similar to the minimized composites, thus confirming the presence of vacancy defects in the final composites. Activated defects disrupt the overall electron–hole symmetry of a carbon nanomaterial and alter its electronic structure, causing an increase in chemical reactivity [58]. The peak located at 517 cm^{-1} ascribed to Si appeared in all the composite curves, further validating that Si maintained its crystallinity and inherent properties.

Figure 7 demonstrates the XPS high-resolution C 1s, O 1s, and N 1s spectra of the composites. Meanwhile, the XPS survey spectra of the fabricated composites in Figure S12 demonstrated strong O 1s and C 1s peaks mainly owing to the presence of a highly graphitic lattice attributed to the OH-GQD and rGO. Relatively smaller peaks for Si 2s and Si 2p imply that the SiNP are substantially coated with a thin OH-GQD layer and then encapsulated within rGO sheets. In addition, the C 1s signal of 0.2OH-GQD@Si/0.2rGO-1 composite shows two strong peaks at 284.74 and 286 eV, which correspond to C–C/C=C in aromatic rings and C–O bonds in −OH and epoxy groups, respectively (Figure 7(a)) [55]. Owing to the −OH functionalization, a slight peak shifting was detected in the C 1s C–C/C=C peak of 0.3OH-GQD@Si/0.1rGO-2 composite with greater OH-GQD content from standard 284.8 eV to the higher binding energy of 284.84 eV. The more electronegative O atoms from the hydroxyl group attached at the edges of OH-GQD pulled more electrons from the graphitic lattice, changing the overall electron cloud density. In the case of the 0.2OH-GQD@Si/0.2rGO-1 composite with lower OH-GQD content relative to GO, the strong van der Waals interaction between graphene interlayers compromised the bond strength with Si; hereby, the binding energy to lower values of 284.74 eV, suggesting a relatively weaker interaction between charged composite parts. Further, it should be noted that the C 1s signals of both composites have intense C–C/C=C peaks accompanied by a significant decrease in the peak intensities of O-containing species associated with the removal of O atoms during thermal processing (Figure S13). Contrarily, 0.3OH-GQD@Si/0.1rGO-2 composite with inherently lower GO content during fabrication produced a weaker C–O peak following thermal reduction (Figure 7(d)). A weak peak at ~289 eV ascribed to O–C=O bonds in −COOH groups are also observed on the composite surfaces [59]. The O 1s signals of the resultant composites also verify the presence of OH-GQD following a low-temperature thermal process, presented by a weak peak of C–OH bonds appearing at ~531 eV (Figures 7(b) and 7(e)) [60]. The N 1s peak detected in the survey spectra and in N 1s scan of the composites (Figures 7(c) and 7(f)), even after thermal treatment, suggests that conducting a low-temperature, one-step OH-GQD annealing/rGO

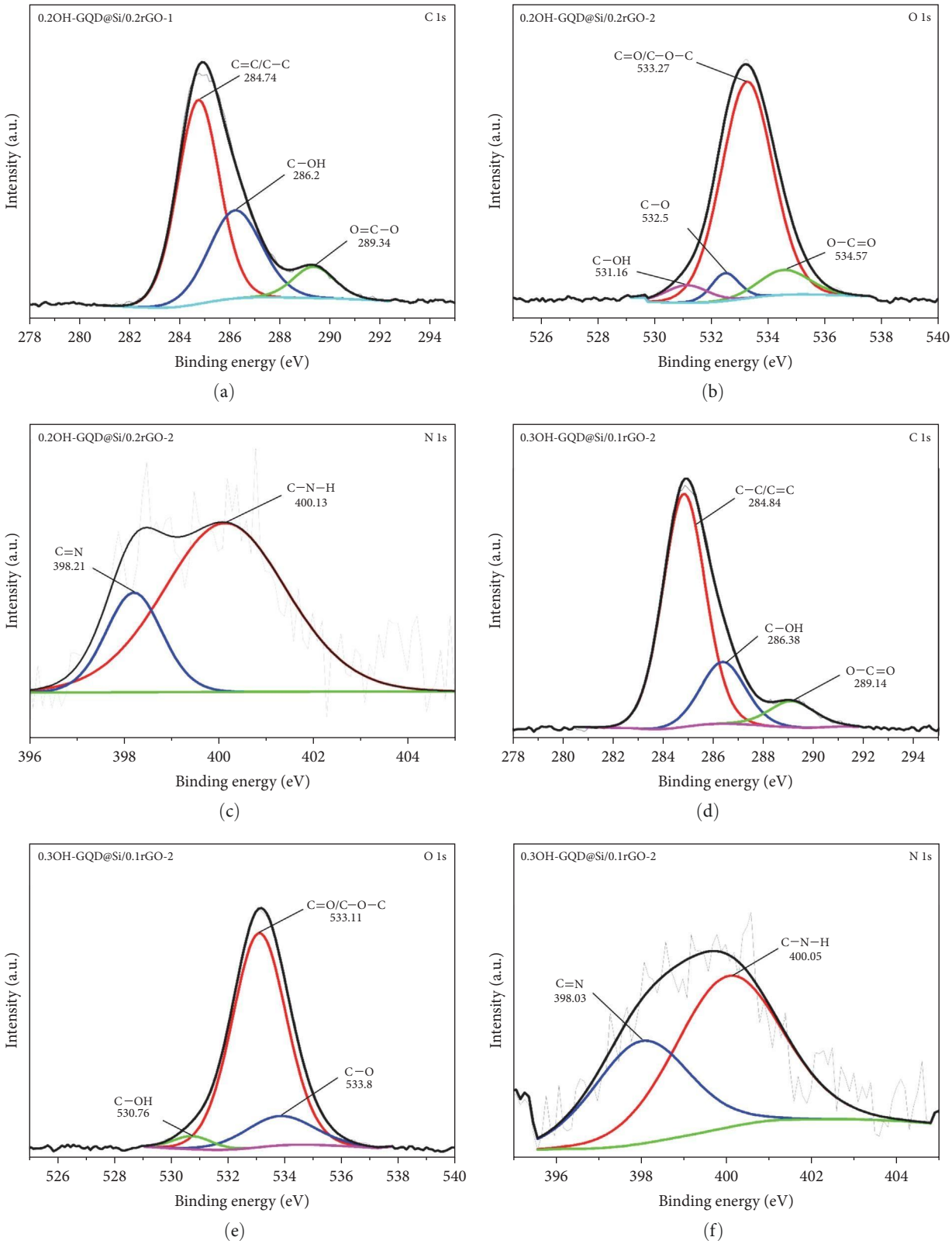

Figure 7: XPS high-resolution C 1s (a, d), O 1s (b, e), and N 1s (c, f) spectra of 0.2OH-GQD@Si/0.2rGO-1 and 0.3OH-GQD@Si/0.1rGO-2 composites, respectively.

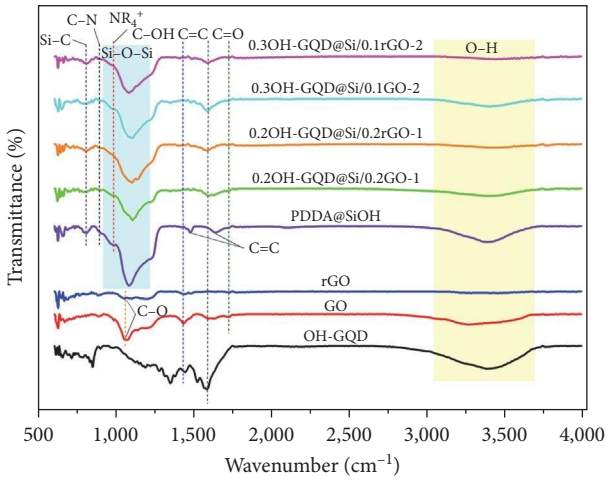

FIGURE 8: FTIR spectra of the various OH-GQD@Si/rGO samples.

reduction is essential for regulating active imine bridges (C–N), also observed in FTIR assessment (Figure 8), which preserves the bridge connection between SiNP, OH-GQD, and rGO.

FTIR analysis was performed to determine the chemical bonds in the samples (Figure 8). The FTIR results are in line with the XPS outcomes in Figures 2(f) and 2(g), where the peaks in the high-resolution Cl 2p and N 1s scans verify the success of the surface modification employing PDDA molecules before composite electrostatic assembly. Representative C–N, NR^{4+}, and C=C peaks detected after PDDA surface modification are all observed in the composites even after thermal processing, subsequently corroborating the existence of remaining active bridges between Si, OH-GQD, and rGO [41, 48]. In addition, the generation of a Si–C peak at ~800 cm^{-1} implies that a carbon shell has been created on the surface of SiNP from successful OH-GQD carbon coating via strong electrostatic interactions with PDDA polymer molecules [33]. Numerous peaks associated with the O-containing functionalities are seen in the GO spectrum (Figure S14). A broad peak is seen at ~3,400 cm^{-1}; it corresponds to the stretching mode vibration of O–H groups superimposed on the O–H stretch of a carboxylic acid (R−COOH) because of the presence of water molecules and alcohol groups. The peak at around 1,720 cm^{-1} is ascribed to the C=O stretching of a−COOH group (−COOH), the peak at 1,224 cm^{-1} corresponds to the C–OH stretch of alcohols, and the peak at 1,080 cm^{-1} is ascribed to the C–O stretching vibrations in a C–O–C bond [59]. Remarkably, the characteristic broad −OH stretching band at ~3,400 cm^{-1}, which is initially detected in the GO spectrum, disappears in the rGO spectrum, while the intensity of other oxygen-containing groups decreases significantly, showing the successful conversion of GO into rGO sheets following the reduction reaction. The disappearance of the −OH stretching adsorption band and reduction in the peak intensity of all oxygen-containing functional groups are also detected in all composites following thermal treatment.

Figure 9 demonstrates the TG/DTA thermograms of the two composites during continuous combustion until a temperature cutoff of 800°C under ambient conditions. The TG/DTA profiles can be partitioned into four phases based on the various composite contents. Phase I showing the weight reduction at ~30 – 120°C corresponds to moisture loss from the PDDA polymer component, followed by the actual polymer decomposition over a broad temperature range until around 280°C [60]. Phase II is marked by sharp weight loss beginning at 400 to ~500°C confirmed by exothermic peaks from 430 to 500°C in 0.2OH-GQD@Si/0.2rGO-1 (Figure 9(a)) and 460–580°C in 0.3OH-GQD@Si/0.1rGO-2 DTA curves (Figure 9(b)) corresponds to the decomposition of the carbonaceous components of the composites. In this phase, most O atoms in the composites were thermally eliminated from the GO layers. The total C content from combusted graphene and OH-GQD in 0.2OH-GQD@Si/0.2rGO-1 composite was 26.5 wt% while 0.3OH-GQD@Si/0.1rGO-2 composite was 28.1 wt%, corresponding to the 1 : 1 ratio of OH-GQD/GO to Si during composite fabrication. Meanwhile, 0.3OH-GQD@Si/0.1rGO-2, which has a greater OH-GQD content, significantly hindered the onset of the Si oxidation process in Phase III as confirmed by an exothermic peak at 580°C, which necessitated a higher temperature range to complete compared with 0.2OH-GQD@Si/0.2rGO-1 (500°C). The Si content of the two composites is ~68.9 wt%, which corresponds with the proportion used during composite synthesis. The last phase, characterized by a steady increase in weight, is associated with the oxidation reaction of the remaining Si component into SiO_x (26.6 wt% in 0.2OH-GQD@Si/0.2rGO-1 and 26.4 wt% in 0.3OH-GQD@Si/0.1rGO-2) owing to direct contact between the carrier gas and the bare Si surface at high temperatures [33]. Notably, measuring the exact combined C contents (from graphene and OH-GQD combined) and Si content may be challenging owing to the possibility of sample weight loss during the annealing/thermal reduction. Nevertheless, carbon nanomaterials, including graphene and OH-GQD, generally combust and are exhausted from the temperature range of 400–550°C, whereas Si remains stable until continuous oxidation occurs from temperatures over 550°C. Thus, a distinction of composite contents can be detected by a rapid loss in sample weight.

In particular, the TG/DTA profile of 0.3OH-GQD@Si/0.1rGO-2 (which has a higher OH-GQD loading) highlights the vital role of the OH-GQD in delaying the oxidation process of the Si particles. This is the product of the successful construction of the OH-GQD coating on the PDDA-modified SiOH nanoparticles via electrostatic connection, which allowed the construction of a composite with a stable structure. The relatively low temperature employed in this research (550°C) permitted the partial reduction of the composites with some of the −OH groups remaining, which regulates the interfacial connection between PDDA@SiOH, OH-GQD lattice, and rGO. A high thermal processing temperature would not have corroborated the construction of an initial GQD layer as a buffer structure for SiNP, as temperatures surpassing 550°C would have combusted most of the O and H atoms, thereby modifying GQD into graphene and soft-carbon materials [41]. Hence, 550°C was set as the thermal processing temperature in this research to build

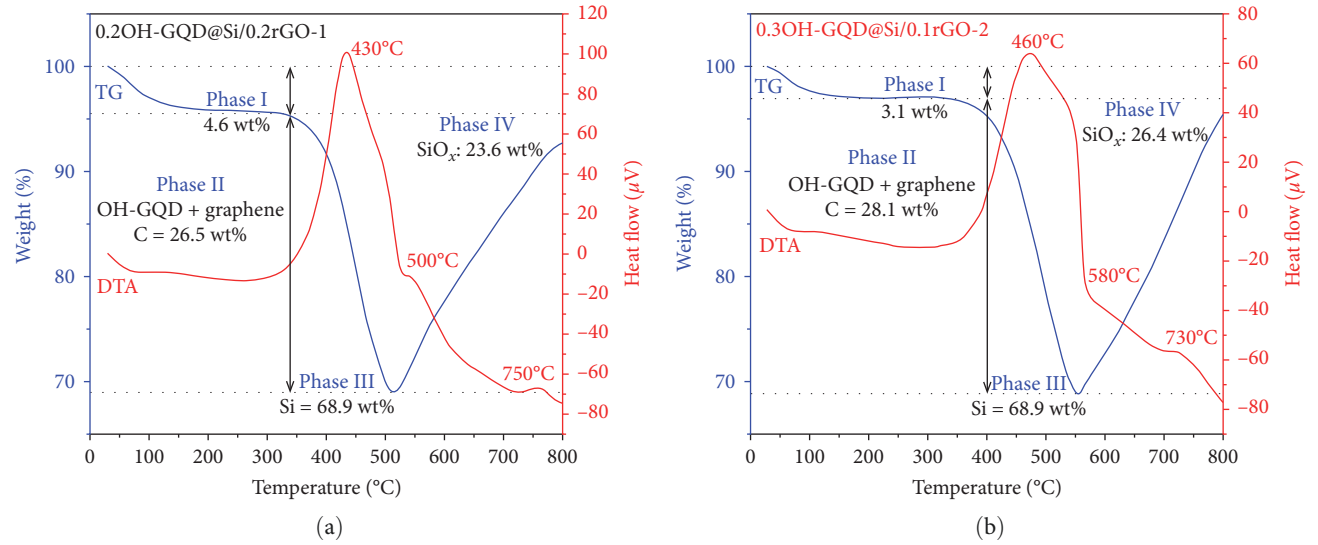

Figure 9: TGA/DTA curves of 0.2OH-GQD@Si/0.2rGO-1 (a) and 0.3OH-GQD@Si/0.1rGO-2 (b) composites.

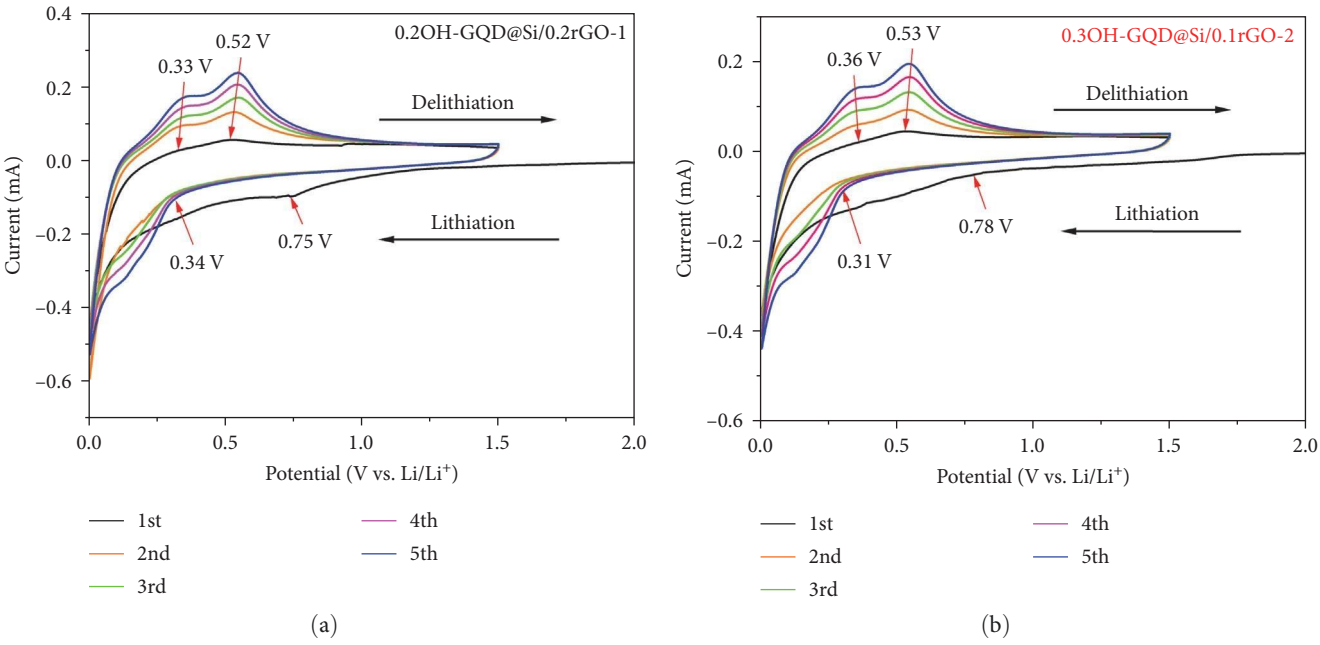

Figure 10: CV profiles of 0.2OH-GQD@Si/0.2rGO-1 (a) and 0.3OH-GQD@Si/0.1rGO-2 (b) electrodes during the initial five cycles.

a GQD coating as initial carbon protection to Si to avert oxidation into SiO_2 while active −OH group functionality yields extra Li^+ ion storage. The shielding effect of the OH-GQD layer on Si is presented by the TGA profiles of the samples (Figure 9). At temperatures over 550°C, Si rapidly oxidizes into SiO_2, as characterized by a sharp rise in the percent mass of each sample.

3.4. Electrochemical Performance. Figure 10 demonstrates the CV curves of the fabricated coin cell utilizing the 0.2OH-GQD@Si/0.2rGO-1 (Figure 10(a)) and 0.3OH-GQD@Si/0.1rGO-2 (Figure 10(b)) composites during the initial five cycles at voltages of 0.01 – 1.5 V (vs. Li^+/Li) at a scan rate of 0.1 mV s^{-1}. Two distinct peaks are observed at 0.34 and 0.75 V during the first cathodic scan (lithiation process) of the 0.2OH-GQD@Si/0.2rGO-1 composite anode. Likewise, two cathodic peaks were observed in the initial CV curve of the 0.3OH-GQD@Si/0.1rGO-2 composite (0.31 and 0.78 V). These two reduction peaks in the cathodic branch of the CV curves are ascribed to the transformation of bulk Si into Li_xSi alloys and other lithiated precipitates (Li_xSiO_y, Li_2CO_3, and Li_2O) yielded in a series of irreversible multistep

Table 1: Summary of phase transformations in SiNP during cycling.

Point in Figure 10	Phase transformation	Chemical reaction [61]
A	SEI formation	$Si + xLi^+ + xe^- \rightarrow Li_xSi$; $x \leq 4$ [52]
B	Lithiation of crystalline Si (c-Si)	$c\text{-}Si + xLi \rightarrow a\text{-}Li_xSi$
C	Transformation to a new phase at <50 mV	$a\text{-}Li_xSi \rightarrow a\text{-}Li_ySi$
D	Delithiation of the phase formed at <50 mV	$a\text{-}Li_ySi \rightarrow a\text{-}Li_{x'}Si + (y - x')Li$
B′	Lithiation of amorphous Si (a-Si) at >0.17 V	$a\text{-}Si + x'Li \rightarrow a\text{-}Li_{x'}Si$
B″	Lithiation of a-Si between 70 mV and 0.17 V	$a\text{-}Li_{x'}Si + x''Li \rightarrow a\text{-}Li_{(x' + x'')}Si$
D″	Delithiation of a-Si at <0.38 V	$a\text{-}Li_{(x' + x'')}Si \rightarrow a\text{-}Li_{x'}Si + x''Li$
D′	Delithiation of a-Si at >0.38 V	$a\text{-}Li_{x'}Si \rightarrow a\text{-}Si + x'Li$

electrochemical reactions between Si and Li^+ ions (Table 1); this outcome follows previous electrochemical studies [62].

Additionally, the peak at 0.75 V in 0.2OH-GQD@Si/0.2rGO-1 and that at 0.78 V in 0.3OH-GQD@Si/0.1rGO-2 are ascribed to the reaction of the electrode material with the electrolyte that caused the irreversible formation of an SEI layer encompassing the surface of the electrode during the discharge process [63]. The cathodic peaks in both composites disappear in the second cycle, implying the formation of a stable SEI layer. The overlap of the CV curves in the second cycle with those in the subsequent cycles validates that the hybridization of the OH-GQD with the SiNP caused improved reversibility, greatly influencing the cycling stability of the anode material. Moreover, two broad oxidation peaks at 0.52 and 0.33 V in 0.2OH-GQD@Si/0.2rGO-1 and at 0.53 and 0.36 V in 0.3OH-GQD@Si/0.1rGO-2 in the subsequent anodic scan (delithiation process) during the first cycle correspond to the partial decomposition of the highest lithiated phase ($Li_{4.2}Si$) and the complete delithiation of the Li_xSi alloys into amorphous Si. A gradual yet steady rise in the intensities of both cathodic and anodic peaks is observed during the subsequent cycle; this is typical of Si-based anode materials and causes a gradual activation of the electrode, which is characterized by an increase in ionic conductivity [64].

The electrochemical performance of the 0.2OH-GQD@Si/0.2rGO-1 and 0.3OH-GQD@Si/0.1rGO-2 composites was evaluated at a low current density of 100 mA g^{-1} for 50 and 100 cycles, as shown in Figure 11(a) with corresponding galvanostatic profiles in Figure 11(b). The specific charge/discharge capacity of 0.2OH-GQD@Si/0.2rGO-1 (Figure S15 for cycle test charge/discharge profiles) and 0.3OH-GQD@Si/0.1rGO-2 during the first cycle is 1,249/1,785 and 1,576/2,229 mAh g^{-1}, which corresponds to an initial CE (ICE) of 69.97% and 70.70%, respectively. Generally, the low ICE of the two composites can be ascribed to the decomposition reaction at the electrode/electrolyte interface; this yielded irreversible products constituting the SEI layer, consuming Li^+ ions in the process, thus lowering their discharge capacities and causing inevitable capacity loss. Remarkably, the CE of the two composites dramatically increased to 96.10% and 97.45% in the second cycle, respectively, and regulated during the subsequent cycles. The rate capability of the two composite electrodes was examined at several current densities in the range of 0.1–5 A g^{-1} (Figure 11(c)). The 0.3OH-GQD@Si/0.1rGO-2 electrode showed a better rate performance than its counterpart at all current densities. The specific capacities of 0.3OH-GQD@Si/0.1rGO-2 electrode were 2,333.32, 1,606.16, 1,557.13, 1,524.25, 1,499.28, and 1,473.28 mAh g^{-1} at the current densities of 0.1, 0.2, 0.5, 1, 2, and 5 A g^{-1}. The 0.3OH-GQD@Si/0.1rGO-2 electrode exhibited an overall better cycling and rate performance owing to the synergistic effects of OH-GQD and rGO hybridization, presenting a double-carbon protection to Si. The corresponding galvanostatic charge and discharge profiles demonstrated overlap of the specific capacities across different current densities demonstrating electrode cycling stability and reversibility (Figure 11(d)) without signs of Li dendritic formation even at a high current density of 5 A g^{-1}, unlike in the rate charge/discharge profile of the 0.2OH-GQD@Si/0.2rGO-1 portraying irregularity in the discharge capacity at increased current densities (Figure S16). Following 50 cycles, the 0.3OH-GQD@Si/0.1rGO-2 composite provided a better cycling performance with 1,300/1,303 mAh g^{-1} charge/discharge capacities corresponding to 99.77% CE compared to its counterpart with only 1,025/1,047 mAh g^{-1} with a CE value of 97.90% (Figure 11(e)). Compared with 0.2OH-GQD@Si/0.2rGO-1, which comprises equal amounts of OH-GQD and GO, 0.3OH-GQD@Si/0.1rGO-2, which has a 2 : 1 OH-GQD/GO loading, shows a better cycling and rate performance in regards to the initial charge/discharge capacity, high-rate loading capability, ICE value, and capacity retention rate. Furthermore, the rate capability of 0.3OH-GQD@Si/0.1rGO-2 surpasses the previously reported literature on utilizing dual-carbon protection to address Si limitations (Figure 11(f)) [33, 48, 59, 65–69]. Table 2 summarizes the cycling and rate performance of the fabricated composites.

The difference in the cycling and rate performances of the two composites can be summarized into three key points: (1) the −OH groups of OH-GQD offered extra storage sites for Li^+ ions, thereby improving the charge/discharge capacities; (2) the electrostatic assembly of the OH-GQD with SiOH enhanced the ionic and electrical conductivity of Si while protecting it from parasitic electrolyte decomposition supporting the formation of a stable SEI; and (3) the rGO sheets encompassing OH-GQD-coated hybrid SiNP offered a continuous pathway for effective electron–ion intercalation across the composite while effectively dispersing Si spheres, thereby resolving SiNP self-agglomeration and causing enhanced structural integrity of the electrode. The shielding effect of the OH-GQD layer, which was previously detected

Table 2: Electrochemical performance of the fabricated composites.

Sample	Low-current density performance (at 0.1 A g^{-1})									High-current density performance		
	Discharge capacity (mAh g^{-1})				Capacity retention (%)		Coulombic efficiency (%)			Discharge capacity (mAh g^{-1})		
	1st cycle	2nd cycle	50th cycle	100th cycle	At 50th cycle	At 100th cycle	1st cycle	2nd cycle	50th cycle	At 1 A g^{-1}	At 2 A g^{-1}	At 5 A g^{-1}
0.2OH-GQD@Si/0.2rGO-1	1,785.35	1,298.26	1,047.19	824.37	99.68	99.49	69.97	96.10	97.90	984.25	966.89	948.19
0.3OH-GQD@Si/0.1rGO-2	2,229.16	1,613.67	1,303.21	1,090.13	99.72	99.59	70.70	97.45	99.77	1,524.25	1,499.28	1,473.28

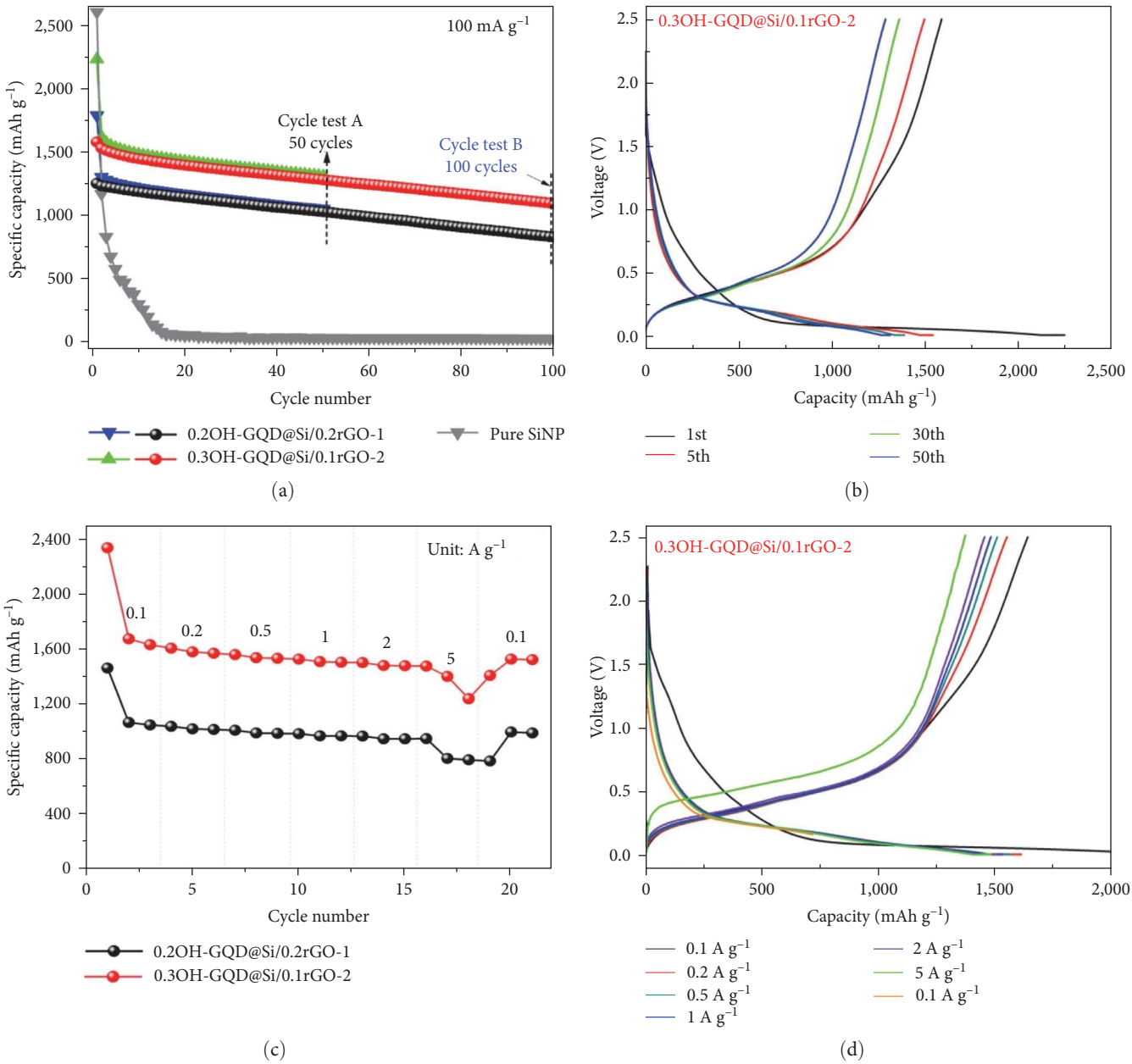

Figure 11: Continued.

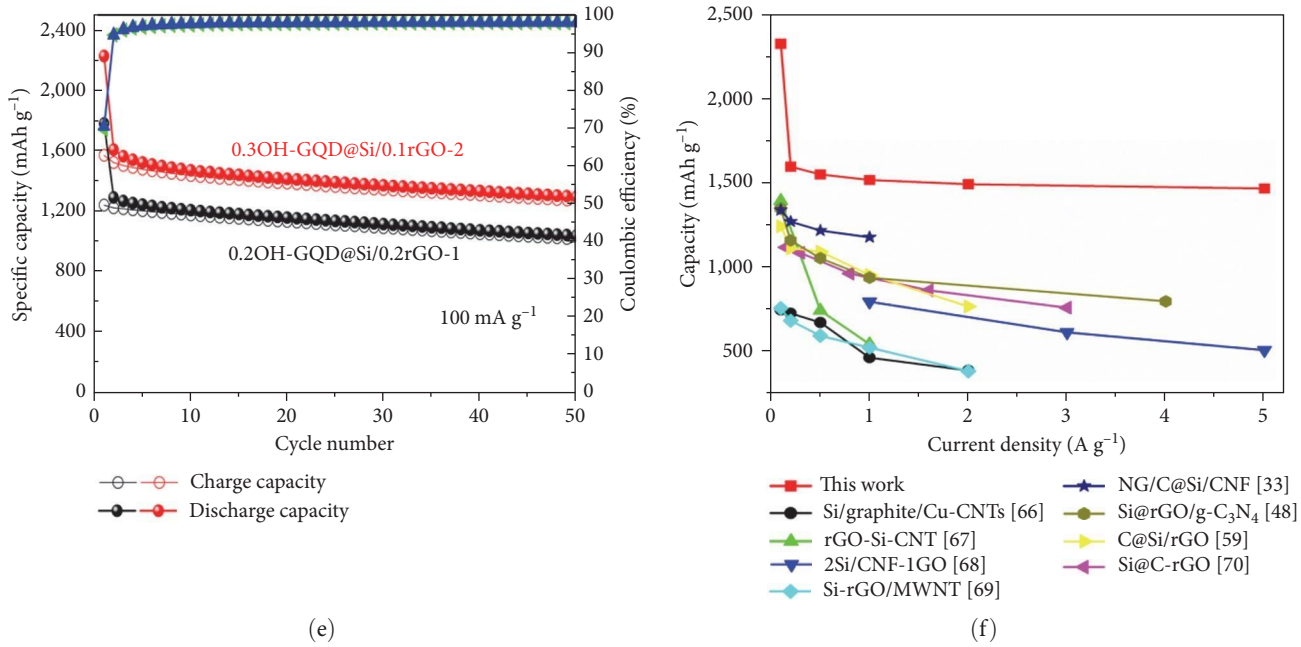

FIGURE 11: Cycling performance of 0.2OH-GQD@Si/0.2rGO-1 and 0.3OH-GQD@Si/0.1rGO-2 (a) with corresponding galvanostatic charge and discharge profiles (b) at a current density of 100 mA g^{-1}. Rate performance of 0.2OH-GQD@Si/0.2rGO-1 and 0.3OH-GQD@Si/0.1rGO-2 (c) with consistent galvanostatic charge and discharge profiles (d) at different current densities. Charge and discharge capacities of 0.2OH-GQD@Si/0.2rGO-1 and 0.3OH-GQD@Si/0.1rGO-2 with corresponding CE at a current density of 100 mA g^{-1} (e). The rate capability of 0.3OH-GQD@Si/0.1rGO-2 composite compared to prior works (f).

in GQD-based composites [43], acted as a buffer system for SiNP, maintained the formation of the SEI film while offering short diffusion pathways for the open transport of Li^+ ions and electrons at the electrode/electrolyte interface through the active −OH sites.

Electrochemical impedance measurements were performed before and after the 30th cycle to describe the factors causing the enhancement in Li^+ storage capacity of 0.3OH-GQD@Si/0.1rGO-2 over its counterpart. The EIS patterns of the fabricated electrodes were recorded at frequencies of 1 mHz to 0.1 Hz and an amplitude of 5 mV, and the obtained Nyquist plots were examined employing the equivalent circuit model shown as insets in Figures 12(a) and 12(b) suitable for the physical structure of the assembled half-cell. The ionic resistance owing to the interaction of the electrolyte solution with the bulk Si (R_s), the resistance of the Li^+ ions during migration between electrodes as it passes through the surface membrane of the SEI layer (R_{SEI}), resistance during charge transfer (R_{CT}), and Warburg impedance (W_z) were considered in the circuit model. The constant phase elements of the cell are the surface film (CPE1) and the double-layer capacitor (CPE2). Nyquist plots were produced before cycling (Figure 12(a)) and after 30 cycles (Figure 12(b)) to scrutinize the formation of SEI layers on both composites and assess the Li^+ storage mechanisms of the electrodes. Table 3 summarizes the fitted parameters acquired from the Nyquist plots of the two composites. The Nyquist plot of each composite before cycling comprises a semicircle in the middle-frequency region, indicative of the charge transfer resistance (R_{CT}) between the electrode and the electrolyte and a slope line in the low-frequency region. As shown in Figure 12(a), the Nyquist plots of the two composites before cycling show similar curve properties, but the plot of 0.3OH-GQD@Si/0.1rGO-2 is a semicircle with a much smaller diameter compared with that of 0.2OH-GQD@Si/0.2rGO-1. Furthermore, the slope of the line in the low-frequency region is larger in 0.3OH-GQD@Si/0.1rGO-2, with a shorter line length, unlike the longer, less steep slanted line of the 0.2OH-GQD@Si/0.2rGO-1 composite. In a classic Nyquist curve for a half-cell, the diameter of the semicircle is the summation of the resistance of Li^+ ions passing through the insulating SEI layer on the surface of the active material (R_{SEI}) and R_{CT}, while the slanted line is directly related to the tortuosity of Li^+ ion diffusion, as given by the Warburg impedance (W_z) [70]. The 0.2OH-GQD@Si/0.2rGO-1 with a greater R_{CT} value of 613.2 Ω than that of 0.3OH-GQD@Si/0.1rGO-2 (239.4 Ω) signifies that there is greater resistance in the 0.2OH-GQD@Si/0.2rGO-1 composite because of the slower diffusion of Li^+ ions as they move around the large graphene sheets. This problem is greatly minimized in the 0.3OH-GQD@Si/0.1rGO-2 composite, which has a smaller semicircle diameter, as depicted in Figure 12(a). Additionally, the 0.3OH-GQD@Si/0.1rGO-2 composite has a relatively steeper, shorter slanted line, which implies faster Li^+ ion diffusion rates. Hence, 0.3OH-GQD@Si/0.1rGO-2, which has a greater loading of OH-GQD (which are small relative to the large GO sheets when coated on the Si surface), enabled the fast transfer of electrons and ions, thereby effectively promoting ionic/electronic conductivity and reducing charge transfer resistance [23].

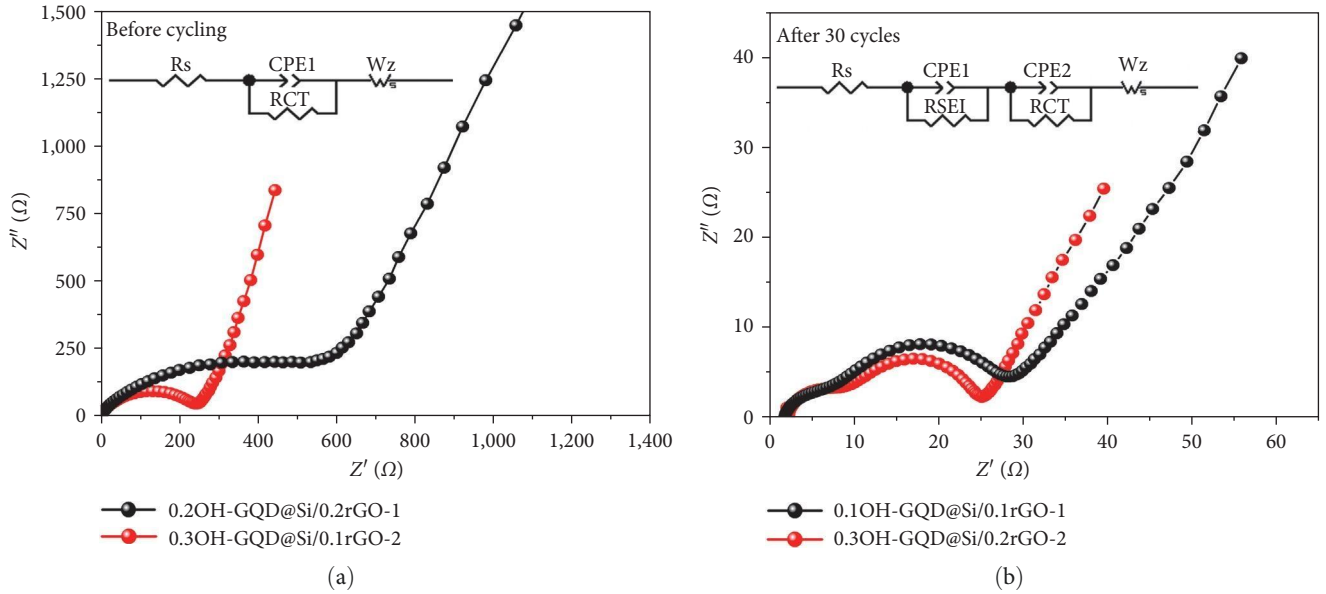

Figure 12: Nyquist plots and electrochemical impedance spectra of 0.2OH-GQD@Si/0.2rGO-1 and 0.3OH-GQD@Si/0.1rGO-2 before cycling (a) and after the 30th cycle (b).

Table 3: Comparison of fitted parameters obtained from Nyquist plots for 0.2OH-GQD@Si/0.2rGO-1 and 0.3OH-GQD@Si/0.1rGO-2 composite anodes.

Sample	Resistance before cycling (Ω)			Resistance after 30 cycles (Ω)		
	R_s	R_{SEI}	R_{CT}	R_s	R_{SEI}	R_{CT}
0.2OH-GQD@Si/0.2rGO-1	–	–	613.2	2.5	4.5	26.1
0.3OH-GQD@Si/0.1rGO-2	–	–	239.4	4.3	3.9	16.5

After 30 cycles, the formation of the SEI layer was measured. Nyquist plots of the two composites in Figure 12(b) show two semicircles in the high-frequency and middle-frequency regions, followed by a slanted line in the low-frequency zone. The R_{SEI} values of 0.2OH-GQD@Si/0.2rGO-1 and 0.3OH-GQD@Si/0.1rGO-2 are 4.5 and 3.9 Ω, respectively. The lower resistance of the 0.3OH-GQD@Si/0.1rGO-2 composite is due to the formation of mechanically stable SEI films on the surfaces of the SiNP coated with OH-GQD layers, which prevented direct contact between the active material and the electrolyte, thereby minimizing parasitic electrolyte decomposition. The R_{SEI} value of the 0.2OH-GQD@Si/0.2rGO-1 composite is higher than that of the 0.3OHGQD@Si/0.1rGO-2 composite, owing to the presence of exposed (uncoated) Si particles. The R_{CT} values of 0.2OH-GQD@Si/0.2rGO-1 and 0.3OH-GQD@Si/0.1rGO-2 are 26.1 and 16.5 Ω, respectively. The lower diameter of the 0.3OH-GQD@Si/0.1rGO-2 plot after 30 cycles implies that the OH-GQD reduced the charge transfer resistance, resulting in fast Li^+ ion diffusion inside the system. This can be attributed to the active sites of the oxygen atoms attached to the edge sites of the OH-GQD, which served as extra storage sites with a strong affinity for Li^+ ions and electrons. The graphene sheets offered a consistent, continuous channel for ion and electron transmission and intercalation to and from the SiNP over the anode material. Large sheets of graphene, in contrast, can substantially impede the efficient transfer of ions and electrons, leading to larger resistance and lower Li^+ ion diffusion rates, as evidenced by the R_{CT} value of the 0.2OH-GQD@Si/0.2rGO-1 composite, which has a higher rGO loading than OH-GQD. The dispersion of the OH-GQD-coated SiNP within the graphene sheets contributed to the overall electrode's structural stability by providing a medium in which SiNP could be dispersed while minimizing particle agglomeration and maintaining the electrode's structural integrity during continuous cycling. As a result, the 0.3OH-GQD@Si/0.1rGO-2 composite, which has a higher OH-GQD mass loading, outperforms the 0.2OH-GQD@Si/0.2rGO-1 composite, which has similar quantities of OH-GQD and GO dispersion.

Further, SEM examination focused on the surface view of the 0.2OH-GQD/0.2rGO-1 and 0.3OH-GQD/0.1rGO-2 electrodes was performed before and after 50 lithiation/delithiation cycles to validate the structural integrity of the composite electrodes, as shown in Figure 13. Figures 13(g) and 13(h) show the good structural stability of the 0.3OH-GQD/0.1rGO-2 electrode compared to its counterpart, which is characterized by fewer cracks on the electrode surface and minimal particle volume expansion. The SiNP morphology was maintained and remained encapsulated within rGO

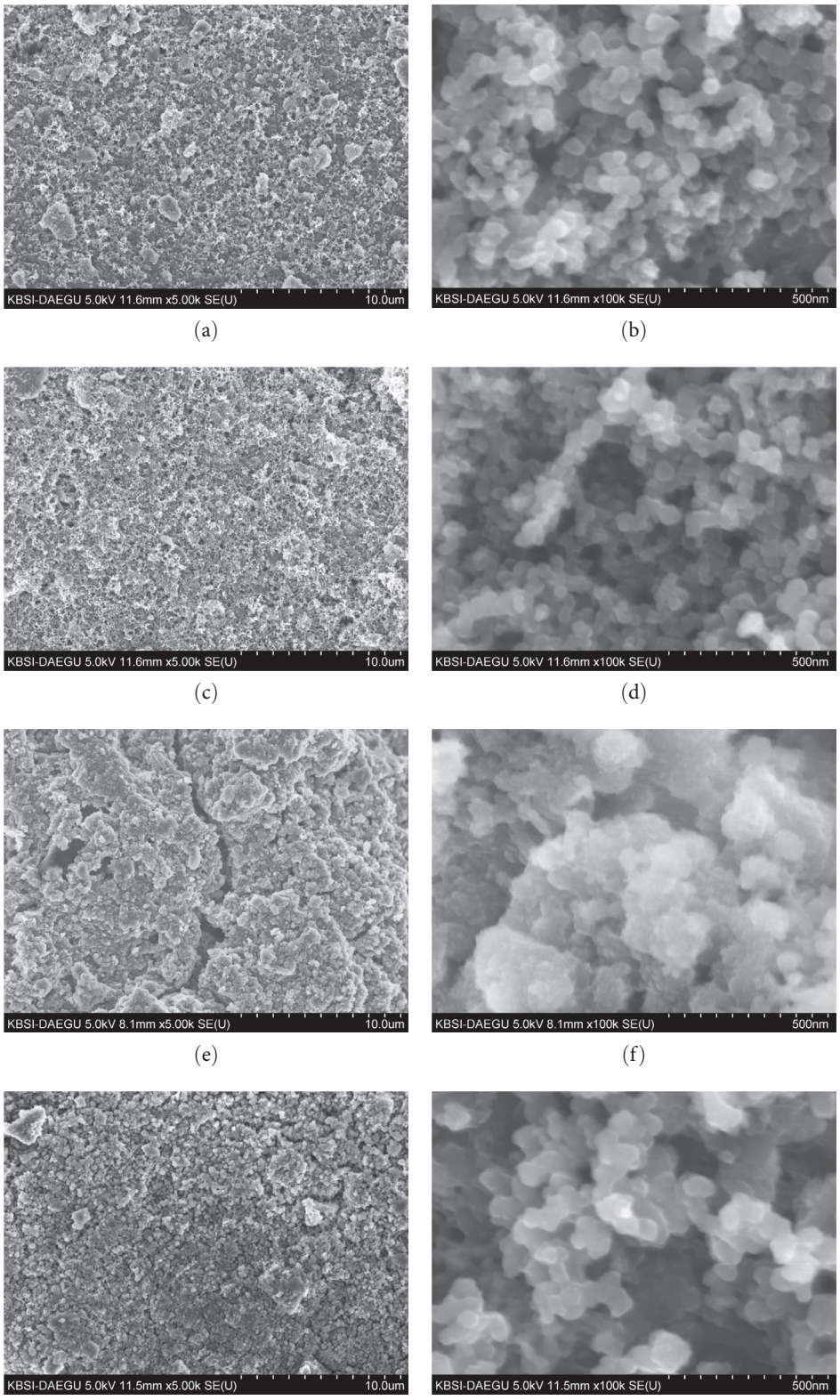

Figure 13: SEM images showing the surface of the 0.2OH-GQD/0.2rGO-1 and 0.3OH-GQD/0.1rGO-2 electrodes before (a–b, c–d) and after 50 lithiation/delithiation cycles (e–f, g–h) at a current density of 100 mA g^{-1}.

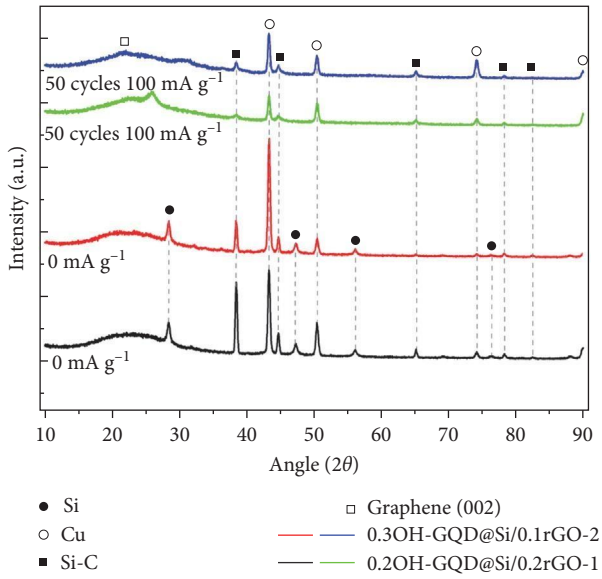

FIGURE 14: XRD thin film analysis of the 0.2OH-GQD/0.2rGO-1 and 0.3OH-GQD/0.1rGO-2 electrodes before and after 50 lithiation/delithiation cycles.

sheets even after cycling. The 0.2OH-GQD/0.2rGO-1 electrode surface, in contrast, showed significant fracture formation, particle aggregation, and considerable Si volume expansion. The relative thickness of the electrodes was evaluated in a cross-sectional view of the electrode to estimate the extent of volume expansion (Figure S17). Before cycling, the 0.2OH-GQD/0.2rGO-1 electrode thickness was 10.1 μm and extended to 13.1 μm. However, it should be noted that due to severe mechanical stress upon cycling, the majority of the composite material has been pulverized to a severe extent, generating cracks and loss of contact with the Cu current collector. Meanwhile, after lithiation, the volume of the 0.3OH-GQD/0.1rGO-2 was not considerably changed, with electrode expansion measured from 13.2 μm (before cycling) to 17.5 μm (after cycling). Most importantly, using the Cu current collector, the entire composite material remained intact, the crack formation was prevented, and particle pulverization was greatly decreased. The structural integrity of the 0.3OH-GQD/0.1rGO-2 after lithiation provides additional evidence that employing a double-carbon protection strategy via OH-GQD carbon coating and further Si encapsulation with rGO resulted in synergistic effects of increased GO coating efficiency improved Si electronic conductivity, uniform Si dispersion, and enhanced mechanical stability from particle expansion to obtain an anode material.

To elucidate the crystallinity of the composite materials, XRD thin film analysis in a low-incident beam angle was conducted on the 0.2OH-GQD/0.2rGO-1 and 0.3OH-GQD/0.1rGO-2 electrodes before and after lithiation/delithiation cycles, as shown in Figure 14. Before lithiation, diffraction peaks were found at $2\theta = 28.4°$, 47.3°, 56.1°, 69.2°, and 76.4° attributed to the (111), (220), (311), (400), (331), and (422) facets of a face-centered cubic Si crystal in both composite spectra (Reference code 00-005-0565; Figure S20). Peaks at 43.3°, 50.5°, and 74.1° attributed to the (111), (200), and (220) facets of cubic Cu crystal (Reference code 01-070-3039; Figure S21) were also identified. After 50 cycles in both electrodes, the individual Si peaks were not detected; instead, peaks at 38.6°, 44.8°, 65.3°, 78.4°, and 82.7° were recorded and indexed to the (111), (002), (022), (113), and (222) facets of cubic silicon carbide (Si–C) (Reference code 98-018-2362; Figure S22). This discovery provides strong evidence that Si has been effectively coated with a carbon coating layer provided by the PDDA polymer molecules electrostatically attracting the OH-GQD. Meanwhile, the large diffraction peak at ~26.0° attributable to the (002) plane of graphene from rGO present before and after cycling shows that the rGO phase was retained. Therefore, the construction of a double-carbon protection layer strategy to address the limitations of Si was realized, and the crystalline structure was maintained as confirmed by the presence of Si–C peaks attributed to conductive OH-GQD coating as an initial carbon protection to Si and a secondary rGO phase which regulated the overall electrode structural integrity.

4. Conclusions

In summary, the scientists used a simple two-step technique to successfully synthesize OH-GQD-coated hydrophilic SiNP electrostatically assembled in an interconnected rGO matrix (OH-GQD@Si/rGO). The effect of the OH-GQD/graphene synergy on the electrochemical performance of OH-GQD@Si/rGO as an anode material for LIBs was also studied. The 0.3OH-GQD@Si/0.1rGO-2 composite outperformed the 0.2OH-GQD@Si/0.2rGO-1 composite in terms of cycling and rate performance, with a high initial discharge capacity of 2,229.16 mAh g^{-1} and a reversible capacities of 1,303.21 and 1,090.13 mAh g^{-1} at 100 mA g^{-1} after 50 and 100 lithiation and delithiation cycles, respectively, equating to a CE value of 99.77%. Even at current densities as high as 5 A g^{-1}, the 0.3OH-GQD@Si/0.1rGO-2 composite was able to deliver a superior reversible capacity of 1,473.28 mAh g^{-1} compared to previous works on Si–C anodes.

The satisfactory electrochemical performance of the 0.3OH-GQD@Si/0.1rGO-2 composite anode is attributed to the following: (1) the shielding effect of the OH-GQD carbon coating reduced ion and electron diffusion paths, resulting in fast charge/ion transfer kinetics via active −OH sites at GQD edges and defects within the lattice; (2) graphene encapsulation as conductive secondary carbon protection to Si served as a buffer system against rapid Si volume changes, preventing direct electrolyte–active material contact and stabilizing the SEI coating; (3) consecutive Si surface modifications via piranha solution treatment improved dispersion stability, while PDDA polymer-induced hydrogen bonds strengthened the grafting mechanism of OH-GQD-coated Si onto graphene sheets, providing continuous transport pathways for effective ion/electron intercalation while maintaining overall electrode structural stability even after cycling; and (4) low-temperature thermal processing enabled one-step OH-GQD annealing concerning vis-à-vis rGO reduction sustained without combusting active bridge connections of Si, OH-GQD, and rGO, promoting the development of OH-GQD coated Si anchored

within rGO network. Our proposed double-carbon protection technique for Si via OH-GQD/rGO hybridization should help to create enhanced Si-based LIB anodes for high-power/high-energy applications.

Data Availability

The datasets generated during and/or analyzed during the current study are available from the corresponding author upon reasonable request.

Conflicts of Interest

The authors declare that they have no conflicts of interest.

Authors' Contributions

A.M. designed, carried out the experiments, curated data, and wrote the main manuscript text. R.C. and H.-H.P. prepared the samples and carried out the experiments. M.J. and H.L. participated in electrochemical measurements in Figures 10–12. As the corresponding author, C.-S.L. was responsible for the submission of the manuscript. All authors reviewed the manuscript. All authors have read and agreed to the published version of the manuscript.

Acknowledgments

The authors acknowledge funding from the National Research Foundation and the Ministry of Education of the Korean Government (Project No.: NRF-2020R1I1A3060565). This work was also supported by the Industrial Fundamental Technology Development Program (Project No.: 20018434), funded by the Ministry of Trade, Industry & Energy (MOTIE) of Korea.

Supplementary Materials

The supplementary material contains additional information on the structural formula of PDDA; edge conformation of GQD; zeta potential values of SiOH, PDDA@SiOH, OH-GQD, OH-GQD@PDDA@SiOH, GO, and OH-GQD@PDDA@SiOH/GO at different concentrations; zeta potential values of PDDA@-SiOH, OH-GQD, and GO at different pH values and IEP determination; Raman peak fitting of GO, rGO, OH-GQD, OH-GQD@Si//GO-1, OH-GQD@Si/rGO-1, OH-GQD@Si//GO-2, OH-GQD@Si/rGO-2, and I_D/I_G values from fitted parameters; XPS survey field spectra and high-resolution scans of composites before and after thermal treatment; FTIR showing rGO thermal reduction; Galvanostic charge and discharge profiles of 0.2OH-GQD@Si/0.2rGO-1 at various cycles and current densities; cross-sectional SEM images of composite electrodes before and after 50 cycles; and JCPDS Reference cards for cubic Si, cubic carbon oxide, cubic copper, and cubic silicon carbide crystal. (*Supplementary Materials*)

References

[1] P. Li, H. Kim, S.-T. Myung, and Y.-K. Sun, "Diverting exploration of silicon anode into practical way: a review focused on silicon–graphite composite for lithium ion batteries," *Energy Storage Materials*, vol. 35, pp. 550–576, 2021.

[2] Y. Chen, Y. Kang, Y. Zhao et al., "A review of lithium-ion battery safety concerns: the issues, strategies, and testing standards," *Journal of Energy Chemistry*, vol. 59, pp. 83–99, 2021.

[3] G. Zubi, R. Dufo-López, M. Carvalho, and G. Pasaoglu, "The lithium-ion battery: state of the art and future perspectives," *Renewable and Sustainable Energy Reviews*, vol. 89, pp. 292–308, 2018.

[4] J. Duan, X. Tang, H. Dai et al., "Building safe lithium-ion batteries for electric vehicles: a review," *Electrochemical Energy Reviews*, vol. 3, pp. 1–42, 2020.

[5] M. A. Pellow, H. Ambrose, D. Mulvaney, R. Betita, and S. Shaw, "Research gaps in environmental life cycle assessments of lithium ion batteries for grid-scale stationary energy storage systems: end-of-life options and other issues," *Sustainable Materials and Technologies*, vol. 23, Article ID e00120, 2020.

[6] C. Hu, H. Ye, G. Jain, and C. Schmidt, "Remaining useful life assessment of lithium-ion batteries in implantable medical devices," *Journal of Power Sources*, vol. 375, pp. 118–130, 2018.

[7] M. Fasahat and M. Manthouri, "State of charge estimation of lithium-ion batteries using hybrid autoencoder and long short term memory neural networks," *Journal of Power Sources*, vol. 469, Article ID 228375, 2020.

[8] X. Li, P. Yan, X. Xiao et al., "Design of porous Si/C–graphite electrodes with long cycle stability and controlled swelling," *Energy & Environmental Science*, vol. 10, no. 6, pp. 1427–1434, 2017.

[9] Z. Chen, J. Hou, Q. Liu, Q. Zhou, H. Liu, and C. Xu, "Graphene quantum dots modified nanoporous SiAl composite as an advanced anode for lithium storage," *Electrochimica Acta*, vol. 318, pp. 228–235, 2019.

[10] X. Zuo, J. Zhu, P. Müller-Buschbaum, and Y.-J. Cheng, "Silicon based lithium-ion battery anodes: a chronicle perspective review," *Nano Energy*, vol. 31, pp. 113–143, 2017.

[11] M. A. Rahman, G. Song, A. I. Bhatt, Y. C. Wong, and C. Wen, "Nanostructured silicon anodes for high-performance lithium-ion batteries," *Advanced Functional Materials*, vol. 26, no. 5, pp. 647–678, 2016.

[12] M. Ge, C. Cao, G. M. Biesold et al., "Recent advances in silicon-based electrodes: from fundamental research toward practical applications," *Advanced Materials*, vol. 33, no. 16, Article ID 2004577, 2021.

[13] K. Guo, R. Kumar, X. Xiao, B. W. Sheldon, and H. Gao, "Failure progression in the solid electrolyte interphase (SEI) on silicon electrodes," *Nano Energy*, vol. 68, Article ID 104257, 2020.

[14] W. Luo, X. Chen, Y. Xia et al., "Surface and interface engineering of silicon-based anode materials for lithium-ion batteries," *Advanced Energy Materials*, vol. 7, no. 24, Article ID 1701083, 2017.

[15] M. Salah, P. Murphy, C. Hall, C. Francis, R. Kerr, and M. Fabretto, "Pure silicon thin-film anodes for lithium-ion batteries: a review," *Journal of Power Sources*, vol. 414, pp. 48–67, 2019.

[16] C. Wang, J. Wen, F. Luo et al., "Anisotropic expansion and size-dependent fracture of silicon nanotubes during lithiation," *Journal of Materials Chemistry A*, vol. 7, no. 25, pp. 15113–15122, 2019.

[17] W. Wei and W. Xiao, "Electrodeposited silicon nanowires from silica dissolved in molten salts as a binder-free anode for lithium-ion batteries," *ACS Applied Energy Materials*, vol. 2, no. 1, pp. 804–813, 2018.

[18] M. Canliang, Z. Wang, Y. Zhao, Y. Li, and J. Shi, "A novel raspberry-like yolk-shell structured Si/C micro/nano-spheres

as high-performance anode materials for lithium-ion batteries," *Journal of Alloys and Compounds*, vol. 844, Article ID 156201, 2020.

[19] H. Jia, X. Li, J. Song et al., "Hierarchical porous silicon structures with extraordinary mechanical strength as high-performance lithium-ion battery anodes," *Nature Communications*, vol. 11, no. 1, Article ID 1474, 2020.

[20] X. Guo, C. Wang, W. Wang et al., "Vacancy manipulating of molybdenum carbide MXenes to enhance Faraday reaction for high performance lithium-ion batteries," *Nano Research Energy*, vol. 1, no. 3, Article ID e9120026, 2022.

[21] G. Liang, X. Li, Y. Wang et al., "Building durable aqueous K-ion capacitors based on MXene family," *Nano Research Energy*, vol. 1, no. 1, Article ID e9120002, 2022.

[22] W.-H. Li, Y.-M. Li, X.-F. Liu et al., "All-climate and ultrastable dual-ion batteries with long life achieved via synergistic enhancement of cathode and anode interfaces," *Advanced Functional Materials*, vol. 32, no. 21, Article ID 2201038, 2022.

[23] B.-H. Hou, Y.-Y. Wang, D.-S. Liu et al., "N-doped carbon-coated $Ni_{1.8}Co_{1.2}Se_4$ nanoaggregates encapsulated in N-doped carbon nanoboxes as advanced anode with outstanding high-rate and low-temperature performance for sodium-ion half/full batteries," *Advanced Functional Materials*, vol. 28, no. 47, Article ID 1805444, 2018.

[24] J.-Z. Guo, H.-X. Zhang, Z.-Y. Gu et al., "Heterogeneous NASICON-type composite as low-cost, high-performance cathode for sodium-ion batteries," *Advanced Functional Materials*, vol. 32, no. 52, Article ID 2209482, 2022.

[25] J. Zhou, Y. Lu, L. Yang et al., "Sustainable silicon anodes facilitated via a double-layer interface engineering: Inner SiO_x combined with outer nitrogen and boron co-doped carbon," *Carbon Energy*, vol. 4, no. 3, pp. 399–410, 2022.

[26] F.-L. Pan, H. Ming, G.-P. Cao, T.-T. Zhang, W.-F. Zhang, and Y. Xiang, "In situ self-nucleophilic synthesis of nano-$Li_4Ti_5O_{12}$/reduced graphite oxide composite with mesopore-oriented porous structure for high-rate lithium ion batteries," *Journal of Central South University*, vol. 29, pp. 2911–2929, 2022.

[27] S. Xing, J. Yang, M. Muska, H. Li, and Q. Yang, "Rock-salt $MnS_{0.5}Se_{0.5}$ nanocubes assembled on N-doped graphene forming van der Waals heterostructured hybrids as high-performance anode for lithium-and sodium-ion batteries," *ACS Applied Materials & Interfaces*, vol. 13, no. 19, pp. 22608–22620, 2021.

[28] P. Sehrawat, A. Shabir, Abid, C. M. Julien, and S. S. Islam, "Recent trends in silicon/graphene nanocomposite anodes for lithium-ion batteries," *Journal of Power Sources*, vol. 501, Article ID 229709, 2021.

[29] H. Shang, Z. Zuo, L. Yu, F. Wang, F. He, and Y. Li, "Low-temperature growth of all-carbon graphdiyne on a silicon anode for high-performance lithium-ion batteries," *Advanced Materials*, vol. 30, no. 27, Article ID 1801459, 2018.

[30] W.-J. Meng, X.-Y. Han, Y.-L. Hou et al., "Defect-repaired reduced graphene oxide caging silicon nanoparticles for lithium-ion anodes with enhanced reversible capacity and cyclic performance," *Electrochimica Acta*, vol. 382, Article ID 138271, 2021.

[31] Y. Zhang, Y. Cheng, J. Song et al., "Functionalization-assistant ball milling towards Si/graphene anodes in high performance Li-ion batteries," *Carbon*, vol. 181, pp. 300–309, 2021.

[32] B. Xiang, W.-L. An, J.-J. Fu et al., "Graphene-encapsulated blackberry-like porous silicon nanospheres prepared by modest magnesiothermic reduction for high-performance lithium-ion battery anode," *Rare Metals*, vol. 40, pp. 383–392, 2021.

[33] R. Cong, M. Jo, A. Martino, H.-H. Park, H. Lee, and C.-S. Lee, "Three-dimensional network of nitrogen-doped carbon matrix-encapsulated Si nanoparticles/carbon nanofibers hybrids for lithium-ion battery anodes with excellent capability," *Scientific Reports*, vol. 12, Article ID 16002, 2022.

[34] K. Lijuan, Y. Yongqiang, L. Ruiyi, and L. Zaijun, "Phenylalanine-functionalized graphene quantum dot-silicon nanoparticle composite as an anode material for lithium ion batteries with largely enhanced electrochemical performance," *Electrochimica Acta*, vol. 198, pp. 144–155, 2016.

[35] X. Liu, Y. Du, L. Hu et al., "Understanding the effect of different polymeric surfactants on enhancing the silicon/reduced graphene oxide anode performance," *The Journal of Physical Chemistry C*, vol. 119, no. 11, pp. 5848–5854, 2015.

[36] F. Wang, X. Qi, L. Mao, and J. Mao, "Aligned ferric oxide/graphene with strong coupling effect for high-performance anode," *ACS Applied Energy Materials*, vol. 4, no. 1, pp. 331–340, 2021.

[37] W. Liu, M. Li, G. Jiang et al., "Graphene quantum dots-based advanced electrode materials: design, synthesis and their applications in electrochemical energy storage and electrocatalysis," *Advanced Energy Materials*, vol. 10, no. 29, Article ID 2001275, 2020.

[38] X. Zhao, Y. Wu, Y. Wang et al., "High-performance Li-ion batteries based on graphene quantum dot wrapped carbon nanotube hybrid anodes," *Nano Research*, vol. 13, pp. 1044–1052, 2020.

[39] X. Li, M. Rui, J. Song, Z. Shen, and H. Zeng, "Carbon and graphene quantum dots for optoelectronic and energy devices: a review," *Advanced Functional Materials*, vol. 25, no. 31, pp. 4929–4947, 2015.

[40] H. Sugimoto, M. Yamamura, M. Sakiyama, and M. Fujii, "Visualizing a core–shell structure of heavily doped silicon quantum dots by electron microscopy using an atomically thin support film," *Nanoscale*, vol. 10, no. 16, pp. 7357–7362, 2018.

[41] A. P. V. K. Saroja, M. S. Garapati, R. Shyiamala Devi, M. Kamaraj, and S. Ramaprabhu, "Facile synthesis of heteroatom doped and undoped graphene quantum dots as active materials for reversible lithium and sodium ions storage," *Applied Surface Science*, vol. 504, Article ID 144430, 2020.

[42] D. Chao, C. Zhu, X. Xia et al., "Graphene quantum dots coated VO_2 arrays for highly durable electrodes for Li and Na ion batteries," *Nano Letters*, vol. 15, no. 1, pp. 565–573, 2015.

[43] J. Kim, W. Jang, J. H. Kim, and C.-M. Yang, "Synthesis of graphene quantum dots-coated hierarchical CuO microspheres composite for use as binder-free anode for lithium-ion batteries," *Composites Part B: Engineering*, vol. 222, Article ID 109083, 2021.

[44] M. Jing, J. Wang, H. Hou et al., "Carbon quantum dot coated Mn_3O_4 with enhanced performances for lithium-ion batteries," *Journal of Materials Chemistry A*, vol. 3, no. 32, pp. 16824–16830, 2015.

[45] W. Zhang, T. Xu, Z. Liu, N.-L. Wu, and M. Wei, "Hierarchical TiO_{2-x} imbedded with graphene quantum dots for high-performance lithium storage," *Chemical Communications*, vol. 54, no. 12, pp. 1413–1416, 2018.

[46] M. Wu, H. Chen, L.-P. Lv, and Y. Wang, "Graphene quantum dots modification of yolk-shell Co_3O_4@CuO microspheres for boosted lithium storage performance," *Chemical Engineering Journal*, vol. 373, pp. 985–994, 2019.

[47] L. Wang, Y. Wang, T. Xu et al., "Gram-scale synthesis of single-crystalline graphene quantum dots with superior optical

properties," *Nature Communications*, vol. 5, Article ID 5357, 2014.

[48] G. Wang, Z. Wen, Y.-E. Yang et al., "Ultra-long life Si@ rGO/g-C_3N_4 with a multiply synergetic effect as an anode material for lithium-ion batteries," *Journal of Materials Chemistry A*, vol. 6, no. 17, pp. 7557–7565, 2018.

[49] K. A. Ritter and J. W. Lyding, "The influence of edge structure on the electronic properties of graphene quantum dots and nanoribbons," *Nature Materials*, vol. 8, pp. 235–242, 2009.

[50] M. H. M. Facure, R. Schneider, L. A. Mercante, and D. S. Correa, "A review on graphene quantum dots and their nanocomposites: from laboratory synthesis towards agricultural and environmental applications," *Environmental Science: Nano*, vol. 7, no. 12, pp. 3710–3734, 2020.

[51] Ç. Ö Girit, J. C. Meyer, R. Erni et al., "Graphene at the edge: stability and dynamics," *Science*, vol. 323, no. 5922, pp. 1705–1708, 2009.

[52] S. Zhang, L. Sui, H. Dong, W. He, L. Dong, and L. Yu, "High-performance supercapacitor of graphene quantum dots with uniform sizes," *ACS Applied Materials & Interfaces*, vol. 10, no. 15, pp. 12983–12991, 2018.

[53] M. Alexandre and P. Dubois, "Polymer-layered silicate nanocomposites: preparation, properties and uses of a new class of materials," *Materials Science and Engineering: R: Reports*, vol. 28, no. 1-2, pp. 1–63, 2000.

[54] X. Bian, Z.-L. Song, Y. Qian et al., "Fabrication of graphene-isolated-Au-nanocrystal nanostructures for multimodal cell imaging and photothermal-enhanced chemotherapy," *Scientific Reports*, vol. 4, Article ID 6093, 2014.

[55] C. Zhao, H. Gao, C. Chen, and H. Wu, "Reduction of graphene oxide in Li-ion batteries," *Journal of Materials Chemistry A*, vol. 3, no. 36, pp. 18360–18364, 2015.

[56] F. Tuinstra and J. L. Koenig, "Raman spectrum of graphite," *The Journal of Chemical Physics*, vol. 53, no. 3, pp. 1126–1130, 1970.

[57] X. Yuan and R. A. Mayanovic, "An empirical study on Raman peak fitting and its application to Raman quantitative research," *Applied Spectroscopy*, vol. 71, no. 10, pp. 2325–2338, 2017.

[58] M.-S. Wang, Z.-Q. Wang, R. Jia et al., "Facile electrostatic self-assembly of silicon/reduced graphene oxide porous composite by silica assist as high performance anode for Li-ion battery," *Applied Surface Science*, vol. 456, pp. 379–389, 2018.

[59] X. Li, Y. Bai, M. Wang et al., "Dual carbonaceous materials synergetic protection silicon as a high-performance free-standing anode for lithium-ion battery," *Nanomaterials*, vol. 9, no. 4, Article ID 650, 2019.

[60] X. Zhou, Y.-X. Yin, L.-J. Wan, and Y.-G. Guo, "Self-assembled nanocomposite of silicon nanoparticles encapsulated in graphene through electrostatic attraction for lithium-ion batteries," *Advanced Energy Materials*, vol. 2, no. 9, pp. 1086–1090, 2012.

[61] J. Shin, T.-H. Kim, Y. Lee, and E. A. Cho, "Key functional groups defining the formation of Si anode solid-electrolyte interphase towards high energy density Li-ion batteries," *Energy Storage Materials*, vol. 25, pp. 764–781, 2020.

[62] C. K. Chan, R. Ruffo, S. S. Hong, R. A. Huggins, and Y. Cui, "Structural and electrochemical study of the reaction of lithium with silicon nanowires," *Journal of Power Sources*, vol. 189, no. 1, pp. 34–39, 2009.

[63] F. Wang and J. Mao, "Extra Li-ion storage and rapid Li-ion transfer of a graphene quantum dot tiling hollow porous SiO_2 anode," *ACS Applied Materials & Interfaces*, vol. 13, no. 11, pp. 13191–13199, 2021.

[64] B. Li, F. Yao, J. J. Bae et al., "Hollow carbon nanospheres/silicon/alumina core–shell film as an anode for lithium-ion batteries," *Scientific Reports*, vol. 5, Article ID 7659, 2015.

[65] T. Xu, N. Lin, W. Cai et al., "Stabilizing Si/graphite composites with Cu and *in situ* synthesized carbon nanotubes for high-performance Li-ion battery anodes," *Inorganic Chemistry Frontiers*, vol. 5, no. 6, pp. 1463–1469, 2018.

[66] M. Fang, Z. Wang, X. Chen, and S. Guan, "Sponge-like reduced graphene oxide/silicon/carbon nanotube composites for lithium ion batteries," *Applied Surface Science*, vol. 436, pp. 345–353, 2018.

[67] M.-S. Wang, W.-L. Song, and L.-Z. Fan, "Three-dimensional interconnected network of graphene-wrapped silicon/carbon nanofiber hybrids for binder-free anodes in lithium-ion batteries," *ChemElectroChem*, vol. 2, no. 11, pp. 1699–1706, 2015.

[68] C. Chae, W. Choi, S. Ji et al., "Electrostatically assembled silicon–carbon composites employing amine-functionalized carbon intra-interconnections for lithium-ion battery anodes," *ACS Applied Energy Materials*, vol. 2, no. 3, pp. 1868–1875, 2019.

[69] D. A. Agyeman, K. Song, G.-H. Lee, M. Park, and Y.-M. Kang, "Carbon-coated Si nanoparticles anchored between reduced graphene oxides as an extremely reversible anode material for high energy-density Li-ion battery," *Advanced Energy Materials*, vol. 6, no. 20, Article ID 1600904, 2016.

[70] W. Choi, H.-C. Shin, J. M. Kim, J.-Y. Choi, and W.-S. Yoon, "Modeling and applications of electrochemical impedance spectroscopy (EIS) for lithium-ion batteries," *Journal of Electrochemical Science and Technology*, vol. 11, no. 1, pp. 1–13, 2020.